IDENTIFYING E AND F LAYER IONOSPHERIC IRREGULARITIES WITH A SCINTILLATION AURORAL GPS ARRAY

BY

VAISHNAVI SREENIVASH

DEPARTMENT OF MECHANICAL, MATERIALS AND AEROSPACE ENGINEERING

Submitted in partial fulfillment of the
requirements for the degree of
Master of Science in Mechanical and Aerospace Engineering
in the Graduate College of the
Illinois Institute of Technology

Approved ______________
Adviser

Chicago, Illinois
May 2018

ACKNOWLEDGEMENT

I would like to express my deep gratitude to Dr. Seebany Datta-Barua, my research advisor. I am always grateful to her for giving me an opportunity to pursue my first research work, under her guidance. This research would not have been done without her patient guidance, enthusiastic encouragement and useful critiques. I also thank my committee members Dr. Boris S. Pervan and Dr. Kevin W. Cassel for accepting to be on my thesis committee and for reviewing my dissertation. Thanks to the Space Weather Lab friends: Yang, Dan, Ningchao, Roohollah, Uriel and Houshine for their constant feedback and help through the completion of this dissertation. A big thank you to Armour College of Engineering for all the support, academically and financially. Also, special thanks to my parents Mr. Sreenivash and Mrs. Prema Sreenivash for allowing me to go miles away from home to do master's degree in the United States of America. My parents are my pillar of strength and I am always grateful for their motivation, care and love.

I thank National Science Foundation (NSF) for funding this research (AGS-1651465). I would like to thank my lab mate Yang Su in particular because his Ph.D thesis forms the base for my research. Thanks to Dr. Donald Hampton of University of Alaska at Fairbanks for providing the pictures of all-sky camera and one of his works served as background for this research. Also, thank Dr. Joshua Semeter for his research on scintillation which gave clear insight about scintillation and helped my research. Thanks to Dr. Bill Rideout for teaching me how to get PFISR data from the Madrigal database and helping resolve the issues I faced while retrieving the data. Thanks to Dr. Roger Varney of SRI for making the PFISR data available.

TABLE OF CONTENTS

LIST OF TABLES

LIST OF FIGURES

LIST OF SYMBOLS

Symbol	Definition
S4	Amplitude Scintillation Index
σ_ϕ	Phase Scintillation Index
PRN	Pseudo Random Noise
IIT	Illinois Institute of Technology
LOS	Line Of Sight
WSN	Weighted Scintillation Number
DOY	Day Of the Year
HH	Hour
MM	Minute
Ne	Electron density
GNSS	Global Navigation Satellite System
ISR	Incoherent Scatter Radar
LL	Loss of Lock
T_e	Electron Temperature
RX	Receiver
TX	Transmitter

ABSTRACT

The Scintillation Auroral GPS Array (SAGA), comprising six kilometer-spaced receivers located in Poker Flat, Alaska, has been deployed for four years to study high latitude scintillation effects on L1 and L2C frequency Global Positioning System (GPS) signals. These scintillations disrupt the GPS signals received on the earth, affecting navigation services. Scintillation is associated with the variations in plasma densities known as irregularities, present in the ionosphere. Research on scintillation has been done from the past using different instruments and techniques, and for multiple purposes. One important prior effort is automated detection of the scintillation of L1 frequency GPS signals. Other successful research includes estimating the drift velocity of irregularities, anisotropy, height and thickness of the scattering layer. It is important to check before studying the properties of irregularities whether the sensors can detect the scintillations happening in the E or F region. In other words, it is essential to check that the sensors are sensitive not only to F region scintillations but also to the E region scintillations.

The purpose of this work is to identify the ionospheric region, E or F, which is responsible for the scintillation on the L1 and L2C GPS signals. The scintillations of these GPS signals are further classified based on the type of scintillation i.e., phase scintillation and amplitude scintillation. The scintillation events are categorized as amplitude, phase, or both on L1 or L2C frequency occurring in the E or F region. Using the automated scintillation detection routine, a complete list of phase and amplitude scintillations on all days for both the frequencies L1/L2C in the years 2014 and 2015 is created. The highly scintillating days for 2014 and 2015 are sorted and the irregularities layer associated with these scintillation events are identified. The Poker Flat Incoherent

Scatter Radar (PFISR) and All Sky Camera images are used to develop the process of identifying the ionospheric region. The electron density from PFISR is assumed to be an essential parameter to determine the E/F layer irregularities. The All Sky Camera provides the red auroral brightness and the green auroral brightness, where red aurora implies F region and the green aurora implies E region.

A summary of a subset of the scintillation events occurring on the highly scintillating days in 2014 and 2015 is provided through this work. It is found that phase scintillation is occurring more predominantly in the high latitudes than the amplitude scintillation. A number of these are attributed to E and F region irregularities. In future, the scintillation events obtained from this work will be used to study the E and F layers irregularities and properties in detail.

CHAPTER 1

INTRODUCTION

The earth is surrounded by layers of gases with each layer having its own composition and specific properties. These layers are collectively termed as the atmosphere and with increasing altitude from the earth's surface they are referred to as: troposphere, stratosphere, mesosphere, thermosphere and exosphere. The troposphere is the lowest part of the atmosphere and exosphere is the last layer enveloping the earth.

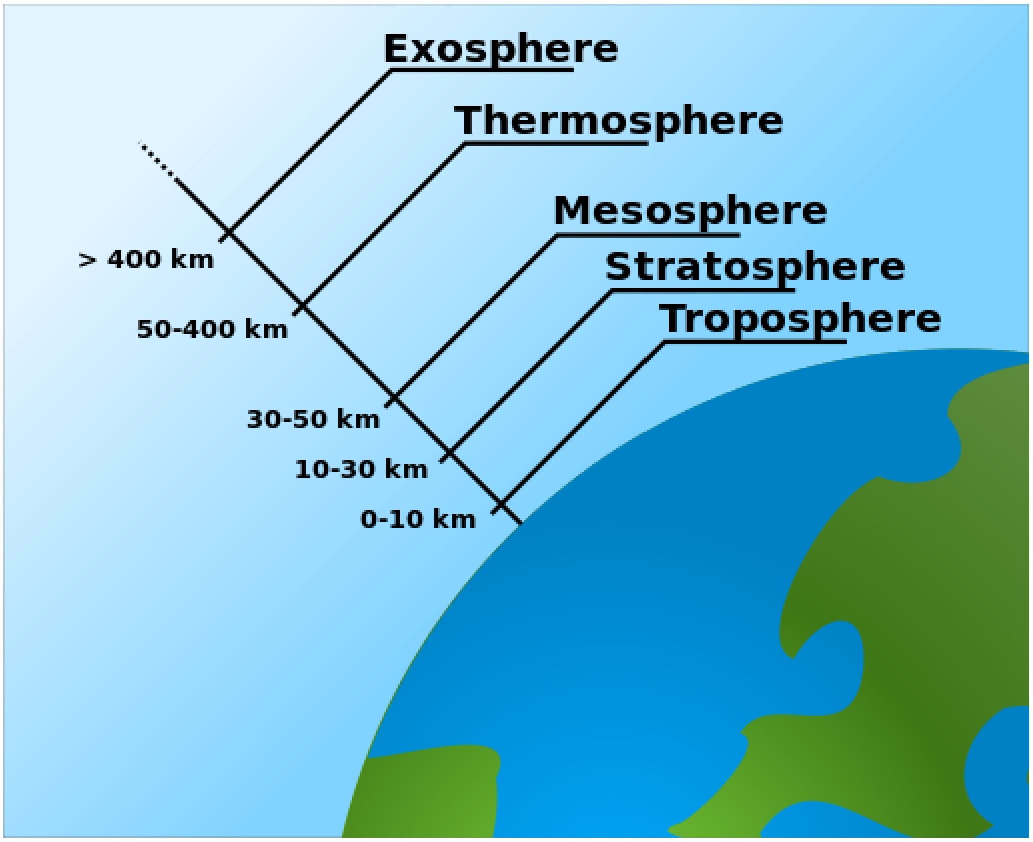

Figure 1.1. Layers of Earth's atmosphere, adapted from [5].

Between the upper part of the mesosphere and the lower part of exosphere, there exists a region of ions and free electrons. The highly energetic ultra-violet and x-ray solar radiation ionize the neutral atoms and molecules present in this region. This plasma layer with ionization is known as the ionosphere. The ionosphere is important in the fields of radio communication, navigation and satellite communication. Depending on the degree of ionization it is primarily classified into D, E and F layers. The D layer is the inner most part of the ionosphere. It is formed in the upper parts of the mesosphere at altitudes between 60 km to about 90 km. The layer lying above D is the E layer formed in the lower parts of thermosphere with altitude ranging from 90 km to 200 km. The outermost layer is the F layer formed in the upper parts of the thermosphere and in the reaches of exosphere. It is spread between an altitude of 200 km to about 1,500 km. During day, the F layer splits into F1 being lower and F2 being upper, as the radiation from the sun is strong enough to create more ions and free electrons than recombine into neutral particles. Figure 1.2 shows the altitude, chemical composition and the electron density of different regions of ionosphere.

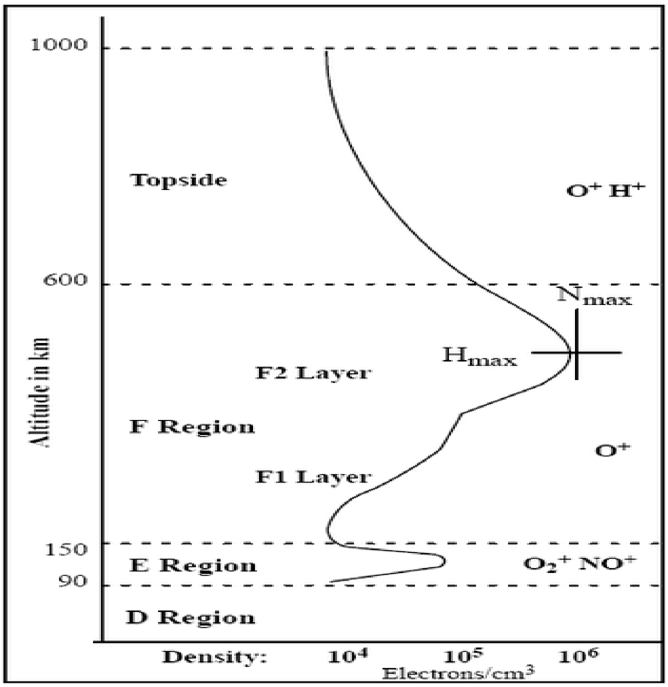

Figure 1.2. Ionosphere Profile. Image Courtesy: National Oceanic and Atmospheric Administration [6]

Basic parameters which describe the state of ionospheric plasma are electron density, electron temperature, ion temperature and the ion composition. The electron density increases with increasing altitude as the impact of solar radiation is more at higher altitudes. Therefore, D layer has the least electron density with magnitude of 10^3 electrons/cm^3 and F layer has the maximum electron density of 10^6 electrons/cm^3. The magnitude of electron density for E layer is in between that in the D and F layers. Above the F layer, the topside ionosphere has decreasing density because the density of neutral particles available to be ionized decreases.

These variations in the electron density of the ionosphere are termed as plasma irregularities, also known as ionospheric irregularities. In general, the ionospheric storm, solar flare, and other space weather events create the plasma irregularities in the ionosphere. The plasma irregularities in the E and F layers affect the areas of communication and navigation.

1.1 Scintillation

As radio waves pass through the ionosphere, they undergo refraction and diffraction due to plasma irregularities present in it. This refraction and diffraction causes rapid fluctuation of the radio waves. This phenomenon is called ionospheric scintillation.

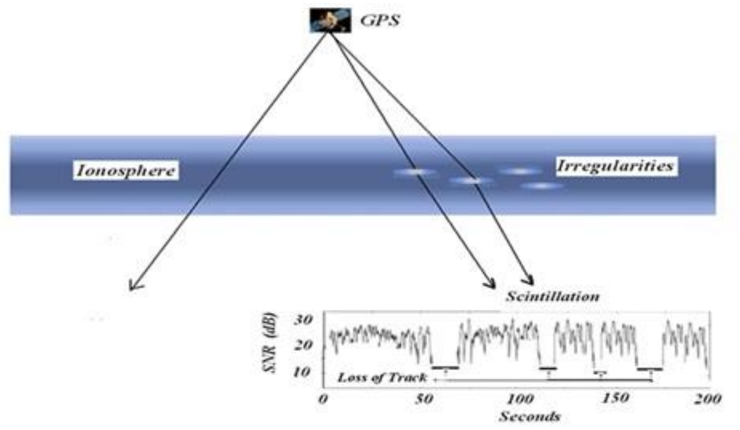

Figure 1.3. Ionospheric scintillation. Image Courtesy: Computational Physics, Inc (CPI) [7].

Rapid fluctuations in the amplitude or intensity of the signal corresponds to amplitude scintillation, and rapid fluctuations in the phase of the signal corresponds to the phase scintillation. The intensity fluctuation and the phase fluctuation of the signal are quantified by the indices S4 and sigmaphi (σ_{ϕ}) respectively. S4 is the amplitude scintillation index and sigmaphi (σ_{ϕ}) is the phase scintillation index. The Global Positioning System is one of the Global Navigation Satellite System (GNSS) owned by the government of United States. GPS comprises 32 satellites with each satellite emitting its own "Pseudo Random Noise" (PRN) to differentiate one from the other. The signals transmitted by these satellites pass through the ionosphere and may undergo scintillation before reaching receivers on earth. Figure 1.4 clearly shows amplitude and phase scintillations of the GPS signal.

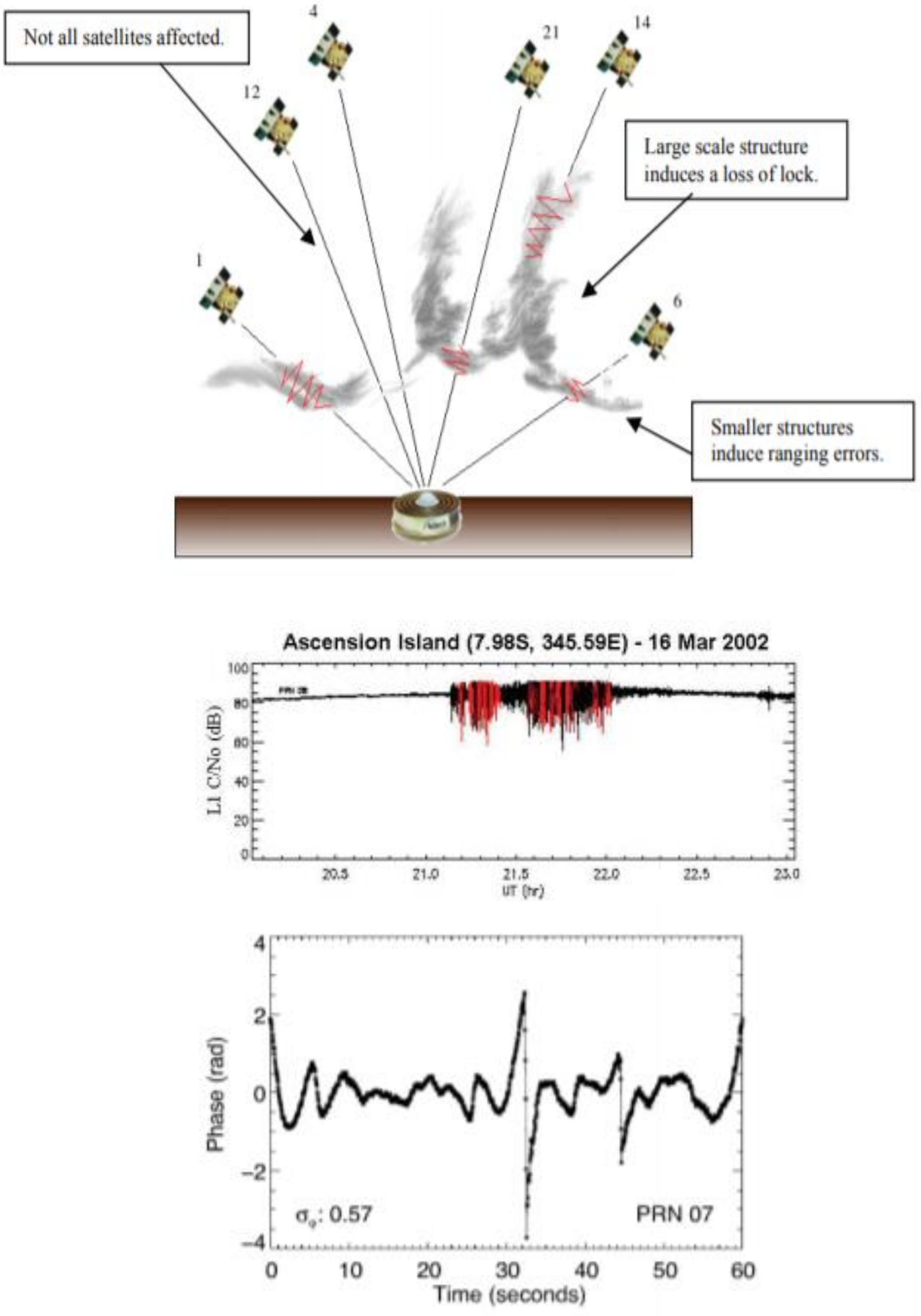

Figure 1.4. Scintillation on GPS signal, showing fluctuations in the amplitude (middle figure) and fluctuations in the phase (bottom figure). Image Courtesy: SBAS Ionospheric working group [8].

GPS receivers require 4 satellites for an accurate position calculation—three for spatial location, and one for time. Losing lock on even a single satellite, due to scintillation can severely degrade the quality of the position. Broadly, this makes scintillation to look as one of the threats to the Global Navigation Satellite System (GNSS).

To suppress the effects of scintillation on GPS signal applications and radio communication, the causes of the irregularities and the properties of the plasma must be analyzed. It is significant to know if there is any difference in irregularities present in the E and F layer in terms of their causes and properties. Before studying the causes, it is required to consider which ionospheric layer (E or F) is responsible for the scintillation. In other words, **it is necessary to find out the ionospheric region (E or F, predominantly) that causes the scintillation.**

1.2 Contributions

The objective of this thesis is to develop the processes to identify scintillations on L1/L2C frequency GPS signals and to determine whether they are due to irregularities in the E layer or F layer of the ionosphere. The contributions of this thesis are reviewed in this section. Each contribution is explained in detail in the following chapters.

1.2.1 Streamed data vs Local data. Two scintillation data sets, namely local data and streamed data are retrieved from Scintillation Auroral GPS Array (SAGA) located in Poker Flat Range, Alaska. It is important to check whether these data sets are identical to decide which data set should be used for this research. Chapter 3 explains the methods of verifying these data sets and justifies choosing the streamed data set for this research.

1.2.2 Automated Phase and Amplitude Scintillation detection. In this work I extend the existing automated L1 frequency phase scintillation detection technique [1] to detect amplitude scintillation. The phase and amplitude detection technique are also applied to L2C frequency. Chapter 3 describes clearly all the new criteria and the process of detecting L1/L2C phase and amplitude scintillations. A complete set of all scintillations that occurred as recorded in the streamed data set at both frequencies in 2014 and 2015 is generated. Also, the top ten days of 2014 and 2015 are ranked based on the severity of scintillation.

1.2.3 Categorising the scintillations as L1/L2 only phase, L1/L2 only amplitude or L1/L2 both phase and amplitude. For the scintillations identified through the previous contribution, an algorithm is developed to find the common time interval between the phase and amplitude scintillation on same day, for the same frequency and same PRN. Chapter 4 describes the algorithm of classifying the scintillations in detail. This algorithm is a tool to explore only phase scintillation, only amplitude scintillation, or both on L1 and L2C GPS frequencies.

1.2.4 Ionospheric Region detection. Chapter 5 discusses the methods used to achieve the objective of this thesis i.e., identifying the region of scintillation (E or F region). Two different methods are approached in determining the altitude of the ionospheric irregularities associated with the scintillations obtained from contribution 2 and classified from contribution 3. The Poker Flat Incoherent Scatter Radar and the All Sky Camera are the instruments used for these two methods respectively. The irregularity layer estimated by these two instruments is compared.

CHAPTER 2

BACKGROUND

In this chapter, the instruments and the data which are used to develop the processes of identifying the region of scintillation and their purposes are explained in detail. Past research which served as a guide to complete and compare the results obtained is also reviewed in this chapter.

2.1 High Latitude Ionosphere

2.1.1 Ionospheric Layers. For historical reasons there are three ionospheric layers that are named the D, E and F regions. These regions do not have well-defined boundaries, and the altitudes at which they occur vary during a day. The parameters that determine these layers are altitude, fraction of ionized particles, degree of ionization, peak electron density and the existence of these layers over time [18]. A fundamental model for each layer was defined by Chapman, in which the solar photoionization from above and increasing atmospheric density from below (for enhanced ion-electron recombination rates) produces an altitude at which these two effects produce the maximum ionization. These are the D, E, and F region density peaks [17]. Unlike the D layer which is present only during the day, the E and F layers are present at day and night. No ionization in the D layer due to lack of solar radiation combined with relatively high atmospheric density, causes it to disappear at night. The electrons and ions recombine in the absence of solar radiation at night in the E and F layers also but incompletely. The E layer gradually weakens as the recombination decreases the plasma density but the F layer is present throughout the night. The F layer has the highest electron density and the strongest ionization among the three and splits in to two layers F1, which is a Chapman layer, and

F2, which is not, during the day [17]. The E and F layers are predominantly important in the area of research, as these two layers appear at night when most scintillations occur.

2.1.2 Aurora Theory. Aurora borealis, popularly known as the northern lights at northern high latitudes, is a display of light in the sky during night. Auroras are caused by the collision of highly energetic particles from space with the atoms and molecules present in the earth’s upper atmosphere. These high energy particles are generated by the earth’s magnetosphere, which is the region of space near earth magnetized by earth's magnetic field and trapped charged particles. The collision makes the atoms and molecules in the earth’s upper atmosphere reach the “excited” state. Photons are emitted by these excited particles when they return to their unexcited state. This emission of photons in the visible spectrum is the aurora.

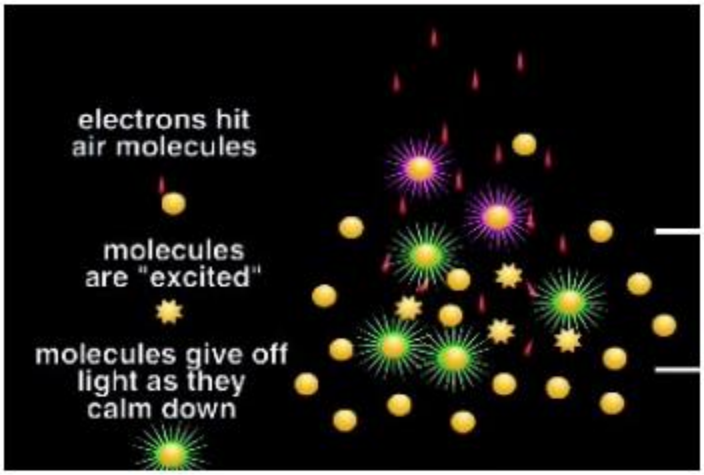

Figure 2.1. Formation of Aurora, adapted from [13].

Auroras are visible in different colors depending on the excited atom or molecule and also the degree of excitation. Green emission is the most commonly viewed auroral color. The green aurora is due to the excitation of atomic oxygen by high energy electrons and is visible as low as 100 km altitude [4]. The red aurora is due to the collision of plasma with neutral atmosphere [4] produced when a low energy electron excites the oxygen atom. This low energy excitation make the red aurora to be formed above 200 km. The nitrogen atom when excited by the electrons emit blue aurora. The light emitted by many different compounds like oxygen and nitrogen atoms at various energy levels include pink and purple [14].

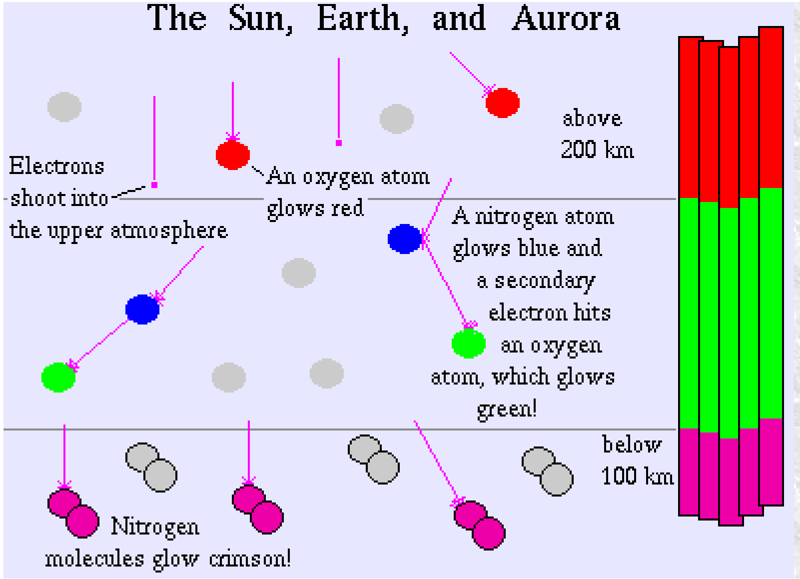

Figure 2.2. Illustration of the causes of different colors of aurora. Reprinted from [14].

Based on the discussion above, in this work we associate the green aurora, which predominantly occurs between 100 km to 200 km altitude, with E – region irregularities. Similarly, the red aurora, which tend to occur above 200 km approximately, in this work we associate with F - region irregularities.

2.2 Instruments and Prior Work

The following are the instruments that provided the data from which the results of this thesis are obtained.

2.2.1 All Sky Camera. The All Sky Camera (ASC) is located at Poker Flat, Alaska. The ASC captures the auroras which are visible in the sky at high latitudes at night.

Figure 2.3. Picture of All Sky Camera at Poker Flat, Alaska. Image Credit: Dr. Donald Hampton [11].

The auroral images for different wavelengths of light throughout a day are available in the form of FITS files, at an interval of 12s. The FITS files can be downloaded from the website of Geophysical Institute and Poker Flat Research Range [16]. The colors of the auroras are significant in determining the region where the scintillation is occurring. The relation between the colors of the aurora and the irregularity region is briefly explained in the section 2.1.2. Chapter 5 describes in detail the procedure to identify the region of scintillation using the All Sky Camera images.

2.2.2 Poker Flat Incoherent Scatter Radar. Radar (RAdio Detection And Ranging) is a system that studies objects by transmitting electromagnetic waves in the direction of the target and the reflected wave from the target is observed. The radar technique used to study the upper atmosphere is called Incoherent Scatter Radar (ISR), as the waves being reflected by the upper atmosphere look like incoherently scattered echoes.

Figure 2.4. Poker Flat Incoherent Scatter Radar. Image credit: SRI. [10]

PFISR is located at 65.12992^{O}N, 145.47104^{O}W, 213 m, Poker Flat Research Range (PFRR), Alaska. This location is known to be “scientifically interesting and logistically friendly” [10], therefore research involving auroral, polar middle and upper atmosphere use PFISR. This is one of the few ISRs with an electronically steerable array, making it stand out from other ISRs. It has been in operation since 2007, and the signals are transmitted in the frequency of 449 – 450 MHz.

The fourth contribution of the thesis requires the data from experiments conducted using PFISR. The electron densities at various altitudes during a day are needed to identify the region where the scintillation has occurred on that day. The Madrigal database provides a platform to access all the experiments carried out by PFISR since 2007 [15]. The ISR basic parameters such as time related parameters, geophysical index, geographic coordinates, etc… are provided by PFISR. This thesis requires the electron density, universal time, altitude, azimuth and elevation from PFISR to identify the region of scintillation. Chapter 5 explains in detail the process of determining the altitude at which the scintillation is occurring on a day based on the electron density obtained from PFISR and also explains, how well the results from PFISR agree with the results from ASC.

2.2.3 Scintillation Auroral GPS Array. The first three contributions of this thesis use the data from Scintillation Auroral GPS Array (SAGA). An array of six Connected Autonomous Space Environment Sensors (CASES) scintillation receivers set up at high latitudes in Poker Flat is called the Scintillation Auroral GPS Array, and it has been in operation since 2013. The dual frequency (L1/L2C) GPS scintillation data is collected through the scintillation receivers set up at Poker Flat Research Range, Alaska. The figure and table below describe the location of these receivers.

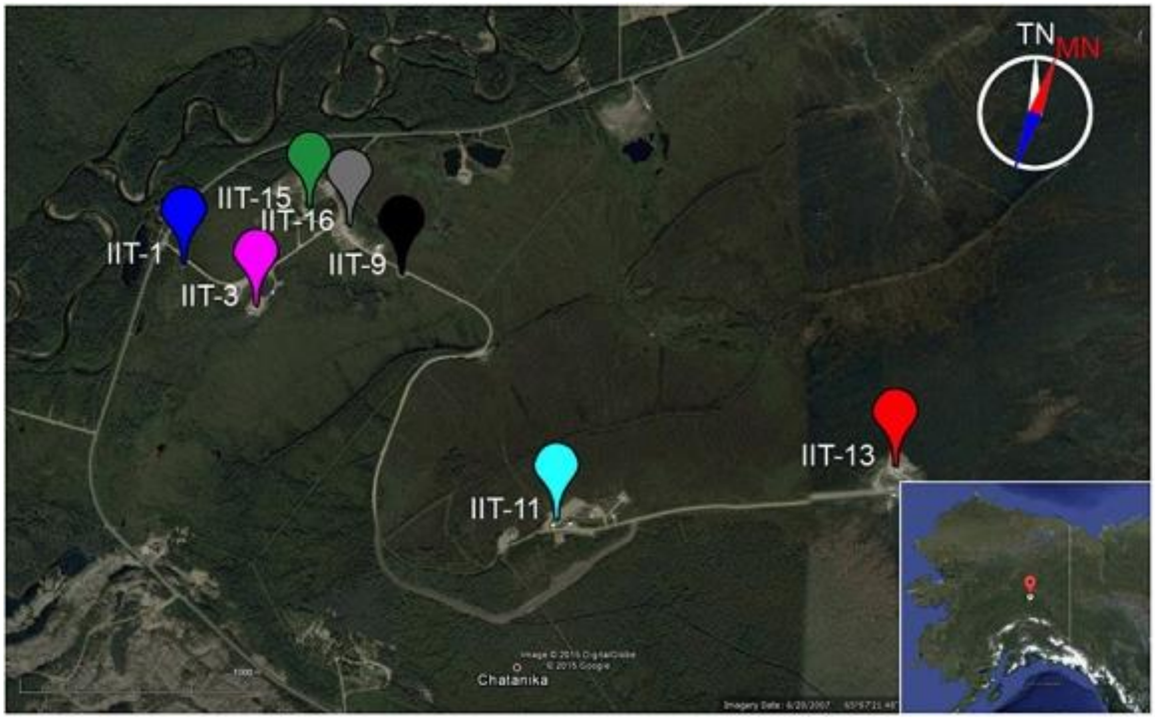

Figure 2.5. Map of array location with true north (TN) to the top. Red compass arrow indicates magnetic north. Image reprinted from [9].

Table 2.1. SAGA Receiver Locations. Reprinted from [2]

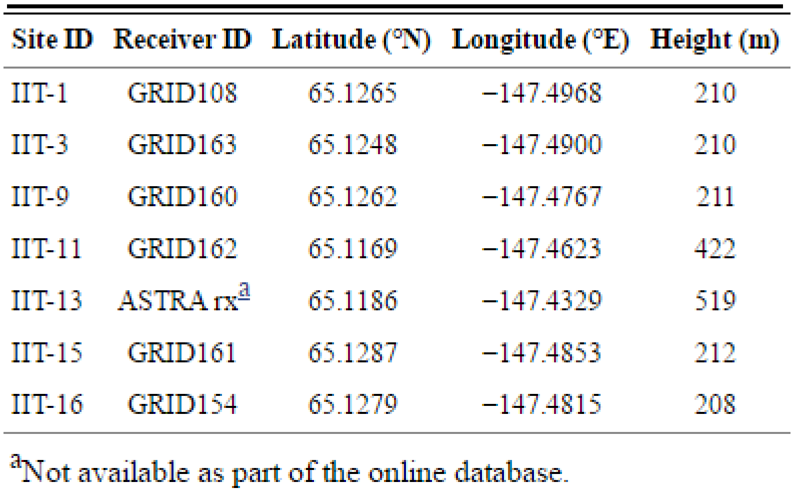

Site ID	Receiver ID	Latitude (°N)	Longitude (°E)	Height (m)
IIT-1	GRID108	65.1265	−147.4968	210
IIT-3	GRID163	65.1248	−147.4900	210
IIT-9	GRID160	65.1262	−147.4767	211
IIT-11	GRID162	65.1169	−147.4623	422
IIT-13	ASTRA rx[a]	65.1186	−147.4329	519
IIT-15	GRID161	65.1287	−147.4853	212
IIT-16	GRID154	65.1279	−147.4815	208

[a] Not available as part of the online database.

The scintillation indices S4 and σ_ϕ which quantify the amplitude and phase scintillation, respectively, are provided by SAGA in the form of text files. These files are known as scintillation files, and they also provide information such as the transmitter identification number (PRN), signal frequency, and local time, in addition to S4 and $\sigma\phi$. Another text file used in this thesis provided by SAGA contains the transmitter (TX) information. This file gives data regarding the transmitters, such as transmitter identification number (PRN), azimuth angle, elevation angle and local time.

Both scintillation and TX information files are available for most days since 2013, with one for each operational receiver on that day. Both these files are readily accessible on a daily basis through the Illinois Institute of Technology, Space Weather Lab, website [9]. These files are important to explore the occurrence of amplitude scintillation or phase scintillation on any day. Chapters 3 and 4 explain how these data files are used for this thesis.

2.2.4 Prior scintillation research using PFISR and ASC data. On December 8, 2013, the phase scintillation was found to occur in the F region [2]. The scintillating time interval was measured using the SAGA data and by applying automated scintillation detection technique [1]. This research used PFISR electron density (Ne) and electron temperature (T_e) data for the beams near the PRN which experienced phase scintillation. It was found that high Ne occurred above 200 km and T_e increased above an altitude of 200 km during the scintillating interval 03:45 to 04:15 UT.

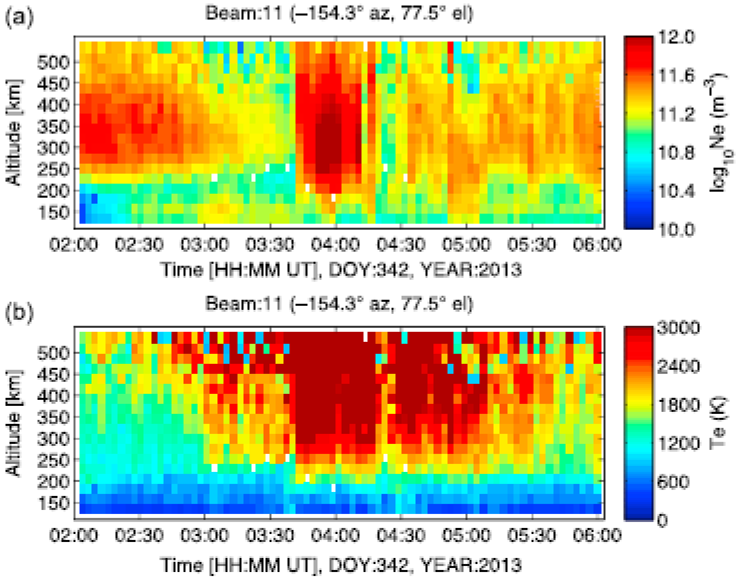

Figure 2.6. a) PFISR Ne and b) PFISR T_e plots of time vs altitude on December 8, 2013 for the interval 02:00 to 06:00 UT and for a radar beam close to scintillating PRN 23. Adapted from [2].

As seen from the above figure, the maximum number of high electron densities had occurred above 200 km altitude, which [2] attributed to soft electron precipitation in the F-region altitude. The prior research [2] concluded that the phase scintillation during 03:45 to 04:15 UT on December 08, 2013 had occurred in the F region based on the observations made from PFISR.

Another paper was found describing phase scintillation observed near Poker Flat, Alaska, on October 7, 2015 attributed to the E-region [3]. The images of the All Sky Camera (ASC) and the electron densities measurements from PFISR were used by this research to identify the region where the phase scintillation occurred on that day. This research compared the altitude of the appearance of aurora during scintillation time with the altitude of the occurrence of highest electron density at the same interval.

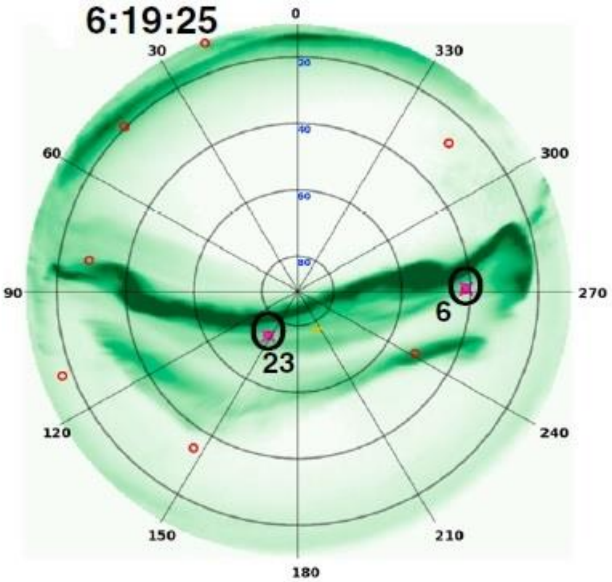

Figure 2.7. All Sky image showing only green line emission (558nm) at 6:19 UT. Black circles indicate the loss of lock events from the respective GPS satellites. Red circles highlight the position of collocated receivers. Image reprinted from [3].

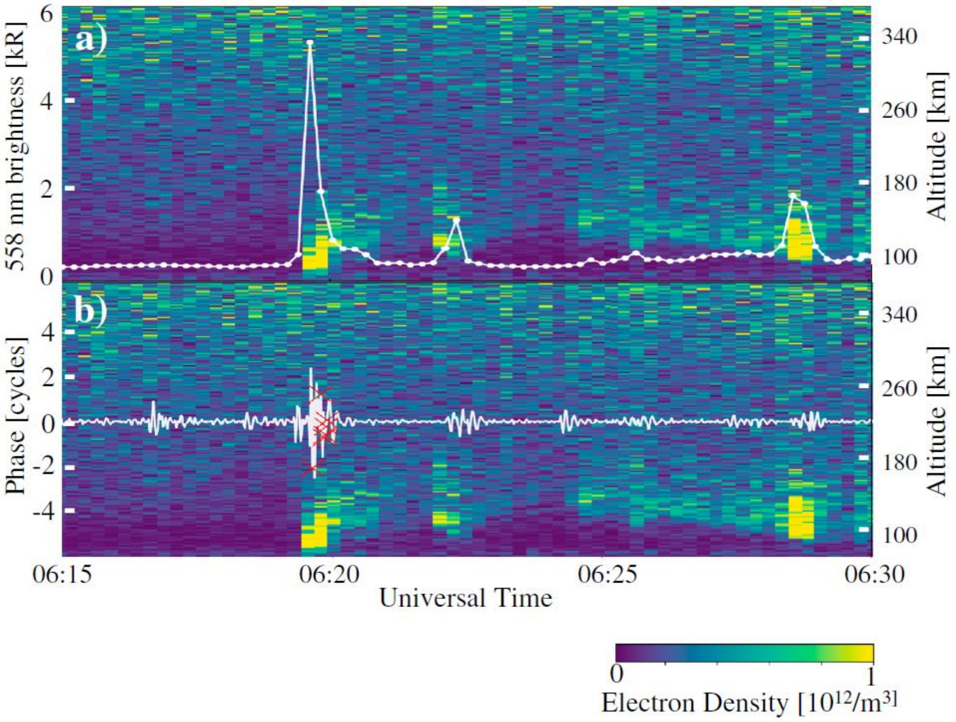

Figure 2.8. a) PFISR Ne and green line brightness plotted against the time and altitude. b) Plot of σ_ϕ values of PRN 23 and L1 frequency, vs time and altitude, red crosses indicate the receiver's loss of lock (LL) which is aligning with the phase scintillation. Image reprinted from [3].

It can be observed from the figure 2.7 reprinted from [3] that the receiver's loss of lock event is linked with the green line emissions. Figure 2.8 a) shows the link between the PFISR Ne measurements and the green line brightness obtained from the auroral images. The green line brightness is witnessed in the altitude range of 100 – 150km and the maximum Ne is also observed below 200 km which is the E region altitude. Based on the ASC and PFISR observations, [3] concluded that the L1 frequency phase scintillation on October 7, 2015 is an E – region scintillation event.

2.2.5 Previous work on scintillation using SAGA. Using the data from SAGA, an algorithm was developed to detect the scintillation and the time intervals during which the scintillation had happened on that day. The algorithm is called "Automated scintillation detection routine". This algorithm was applied to all the days in the year 2014 and a list of top twenty highly scintillating days were found. This automated scintillation detection routine was initially developed to detect only L1 frequency phase scintillations. L1 frequency phase and amplitude scintillations, quick look plots for every receiver are publicly available on a daily basis at [12]. The following figures are examples of S4 and σ_ϕ quick look plots for March 2, 2018.

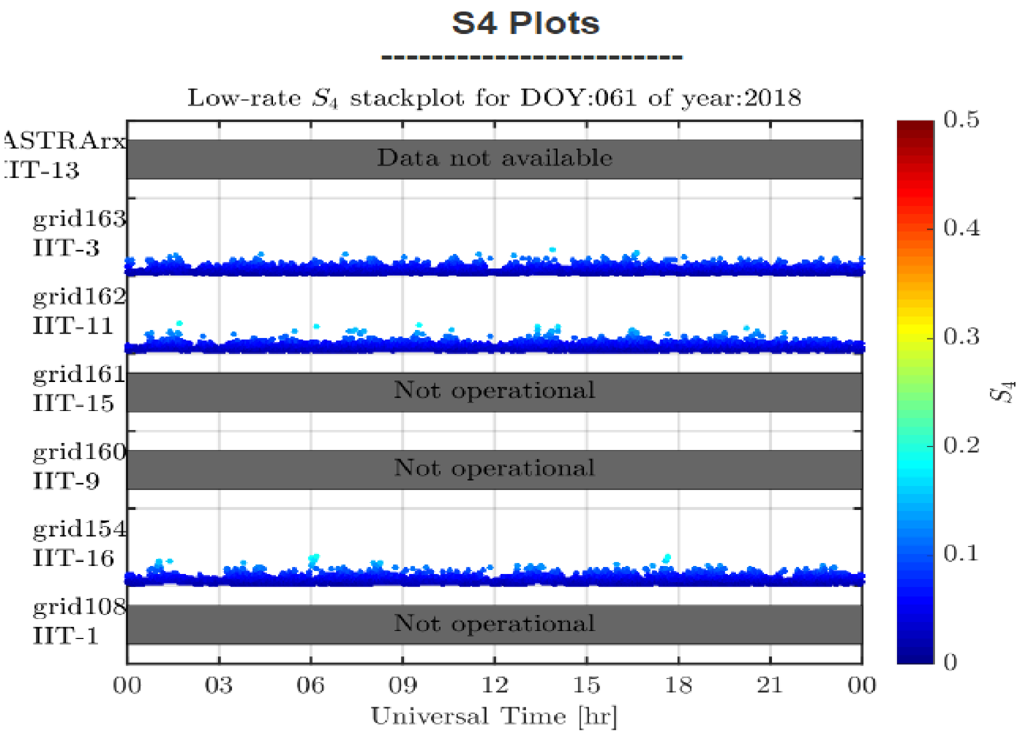

Figure 2.9. Quick look plot of S4 on March 02, 2018. [12]

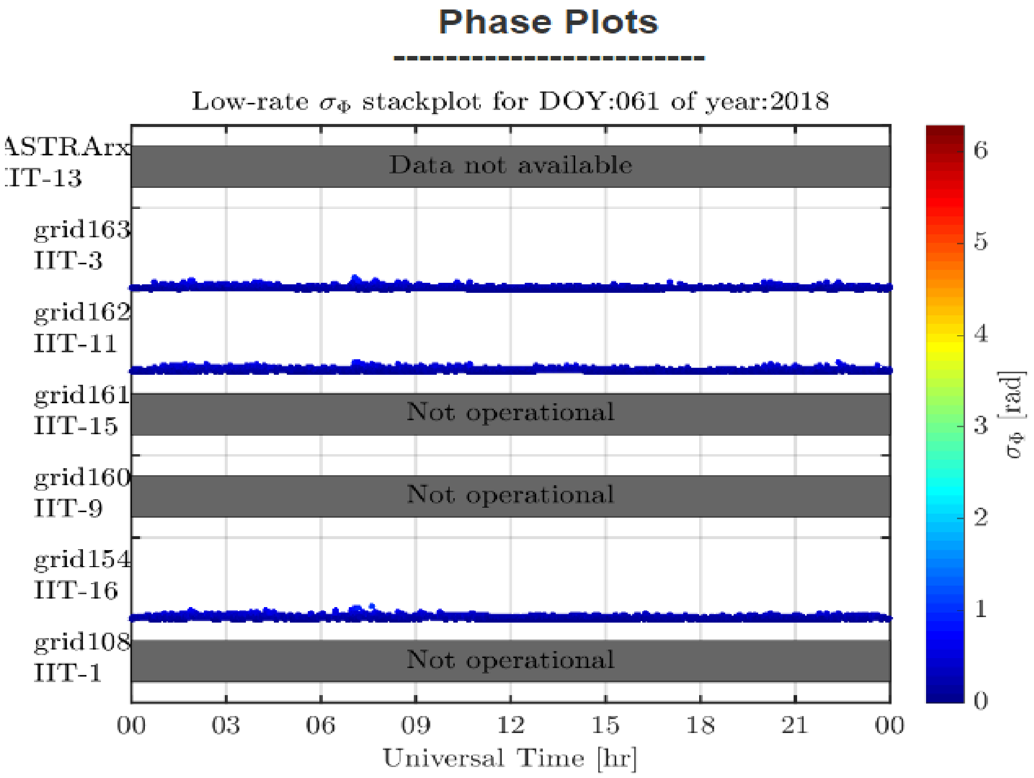

Figure 2.10. Quick look plot of σ_ϕ on March 02, 2018. [12]

CHAPTER 3

SCINTILLATION DATA AND DETECTION

In this chapter, the locally stored and network streamed scintillation data types from the GNSS array SAGA are discussed. A comparison of these data types is carried out to determine whether they are identical. If they are, either set may be used. If not, then one set must be chosen or both combined for the subsequent analysis to be as comprehensive as possible. Also, the application of the automated scintillation detection routine explained in the previous chapter will be adapted for use in this work.

3.1 SAGA Data

As mentioned in the chapter 1, the Scintillation Auroral GPS Array (SAGA) provides the scintillation and the transmitter (TX) data in two text files, the scint.log file and txinfo.log file, respectively. These are publicly available from the Illinois Institute of Technology, Space Weather Lab website [9]. The scintillation file contains time stamped scintillation measurements namely S4, σ_ϕ, GPS frequency, transmitter identification number, etc. The TX information contains time stamped transmitter information such as azimuth and elevation angle of each GPS satellite at each timestamp.

The scint.log and txinfo.log files are available from two different data streams (see Figure 3.1 for a cartoon of the data flow). The data from the SAGA receivers are stored locally at PFRR on an external hard drive attached to each receiver (RX); these are referred as the “local” data. The external hard drives are shipped about once a year when full to IIT, at which time the local data are copied to the server. When there is a network connection, data from SAGA is streamed continuously to a server at Illinois Institute of

Technology, Chicago and is called the “streamed” data. The local data stream has about one year latency; the streamed data are available with one day latency.

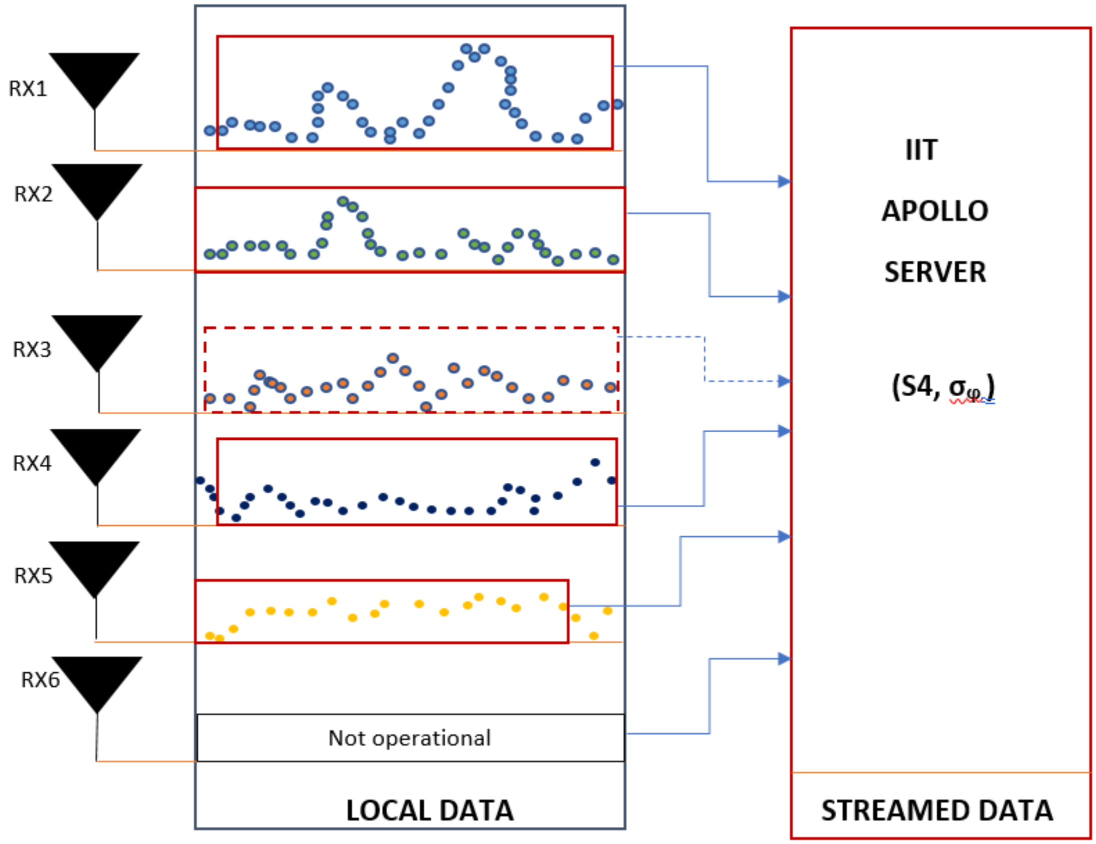

Figure 3.1. Illustration of local and streamed data.

From Figure 3.1 it can be seen that the signal from each of the operational receivers is stored at Poker Flat in a hard drive as local data and some or all of the signal received is streamed to the IIT server as streamed data. One of the receivers i.e., RX6 was not operational on a day so neither local nor streamed data are available. The signal from RX3 is not streamed to the IIT server because of a network disconnection. Since the data from receiver RX3 is not streamed, only local data is available for the receiver RX3.

Before detecting the scintillating time intervals for a day, it is important to verify whether the local and the streamed data are identical or not, when data from both data streams exist (see Figure 3.2 for an illustration). In other words, do the local and streamed data sets sample the data stream at the same time or different times?. This analysis is done to determine which data set to be used for this research, and it constitutes the first contribution of this thesis.

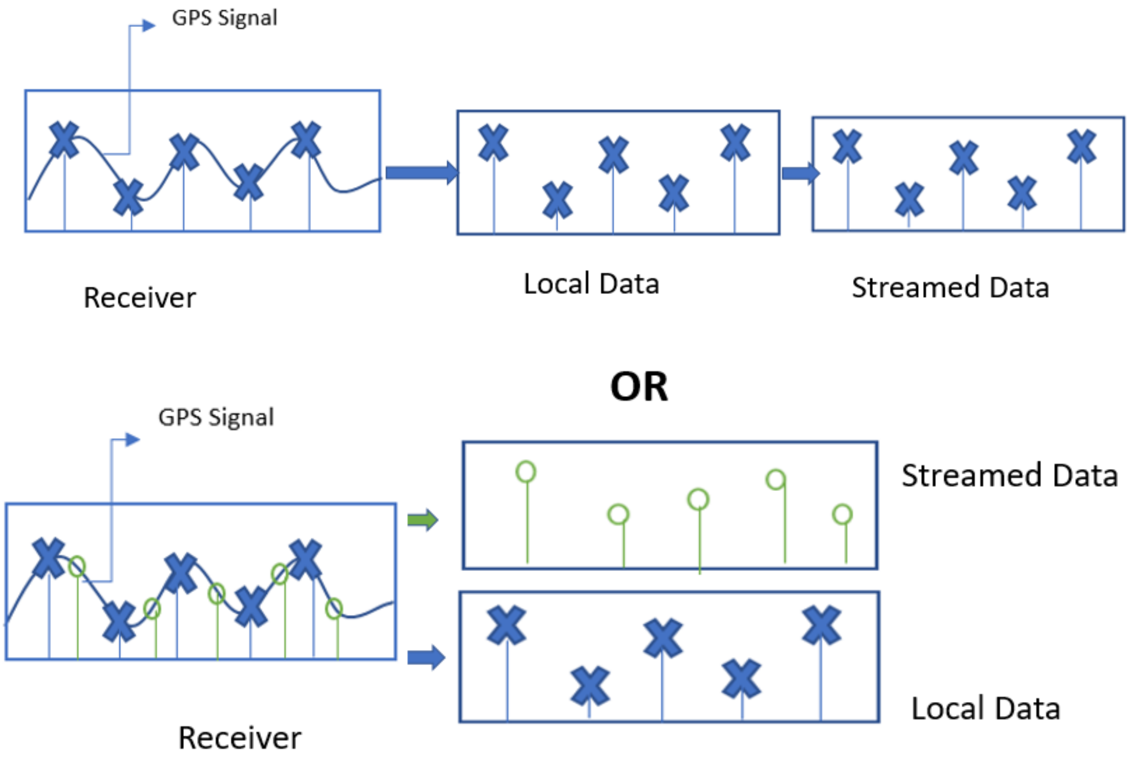

Figure 3.2. Illustration of the question of whether the local data and the steamed data are same. a) Shows that the local and the streamed data are same by picking up the same data points from the receiver signal. b) Shows the local and streamed data are different by picking up different data points.

This question is answered by comparing the scint.log data from the local data set, and the scint.log file from the streamed data set. The following flow chart describes the method used to compare the local and streamed data.

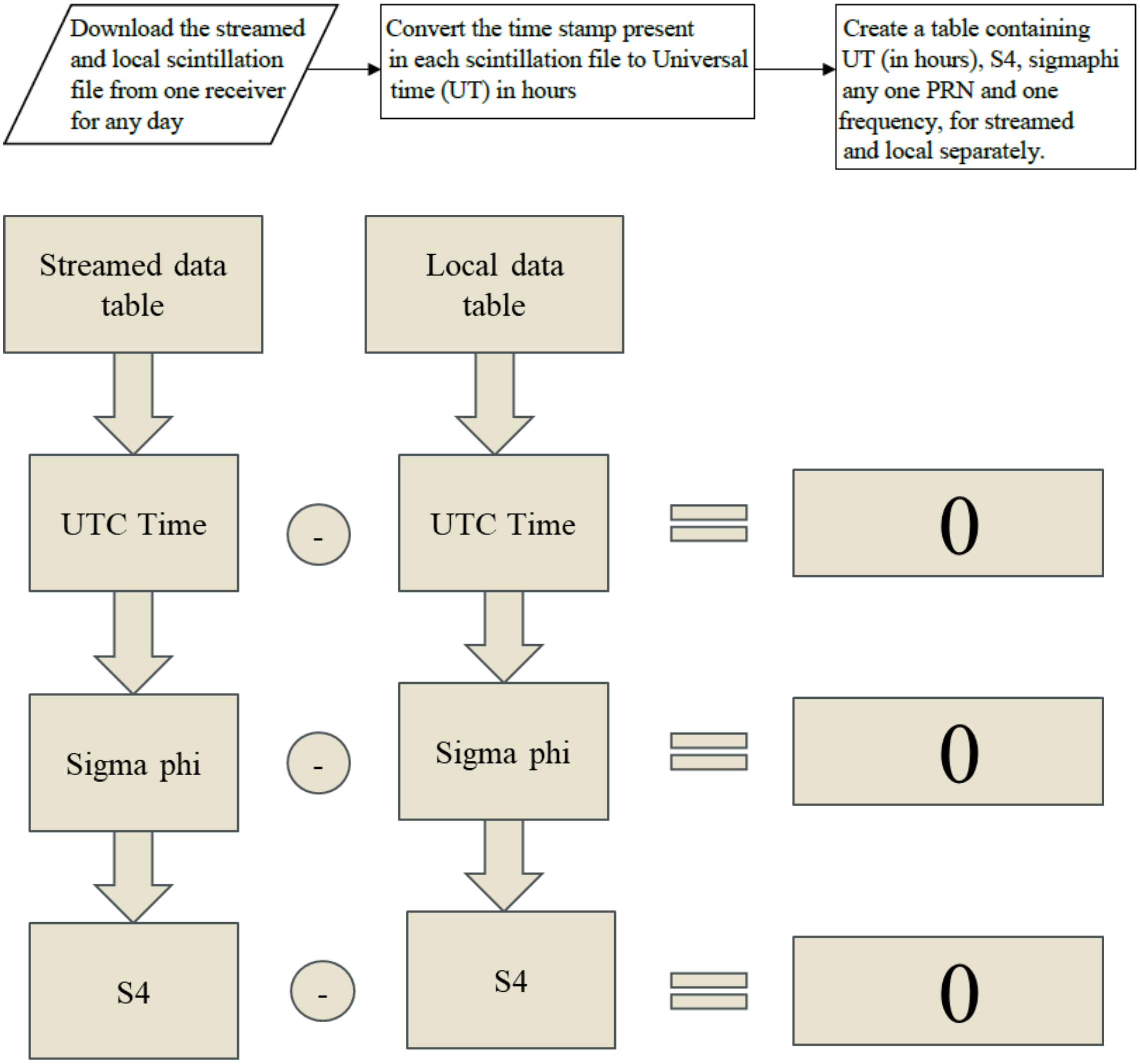

Figure 3.3. Illustration of the process of determining the difference between local and streamed data set.

The scintillation data of one frequency for only one satellite from one receiver is considered for this verification. Two different tables for streamed and local data are created, containing the UTC (in hours), S4 and σ_ϕ. The corresponding columns from both the tables are subtracted to check whether they are same for each PRN or is there any difference in their value.

The result showed that the difference between them is zero as illustrated in the above Figure 3.3. To visually prove this result, the S4 and the σ_ϕ values from the streamed and the local data, at each timestamp from one receiver, for one frequency and one PRN are plotted separately. The figures below clearly explain the result obtained.

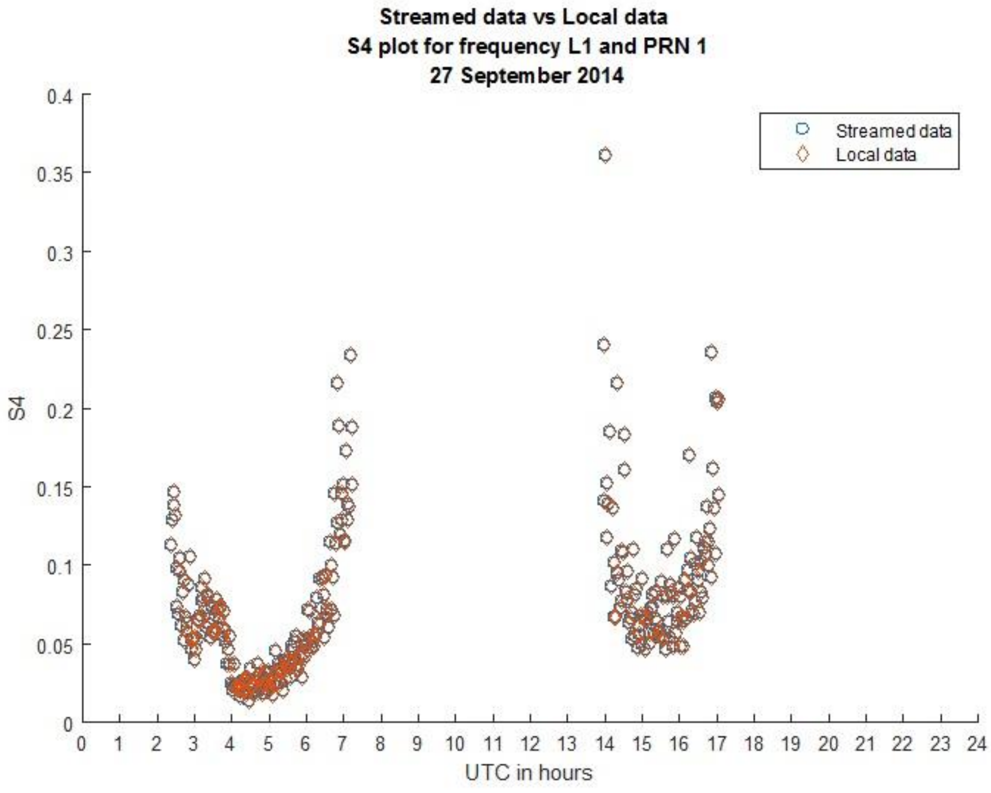

Figure 3.4. S4 values vs time from streamed and local data for L1 frequency, PRN 1 and RX 108 on September 27, 2014.

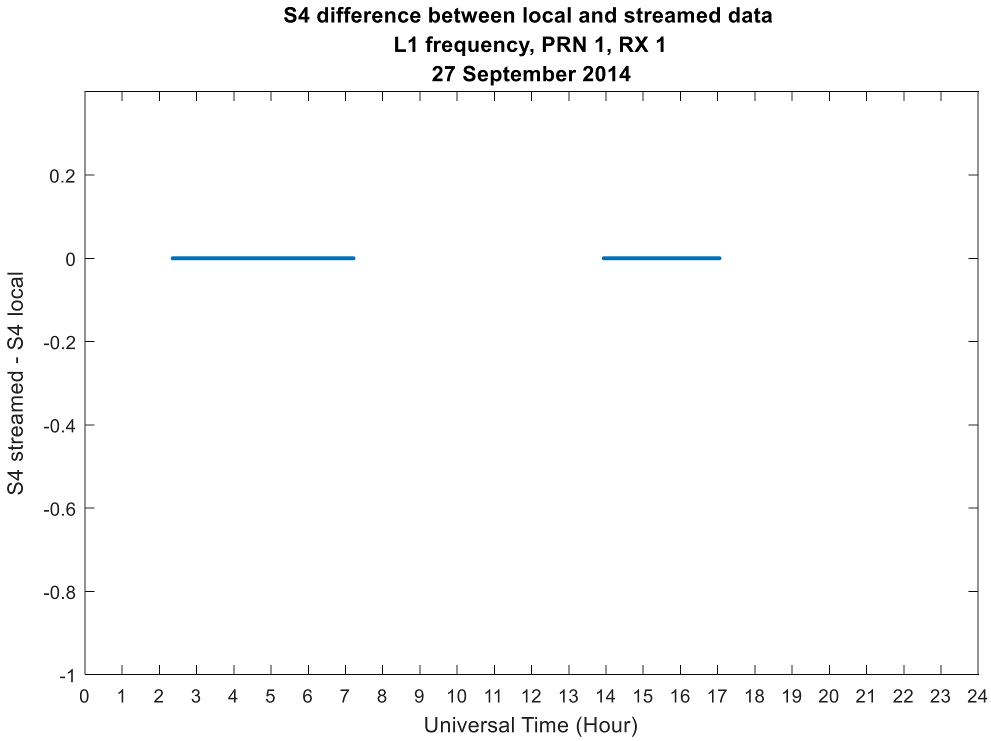

Figure 3.5. Difference of S4 values between streamed and local data vs time for L1frequency, PRN 1 and RX 108 on September 27, 2014.

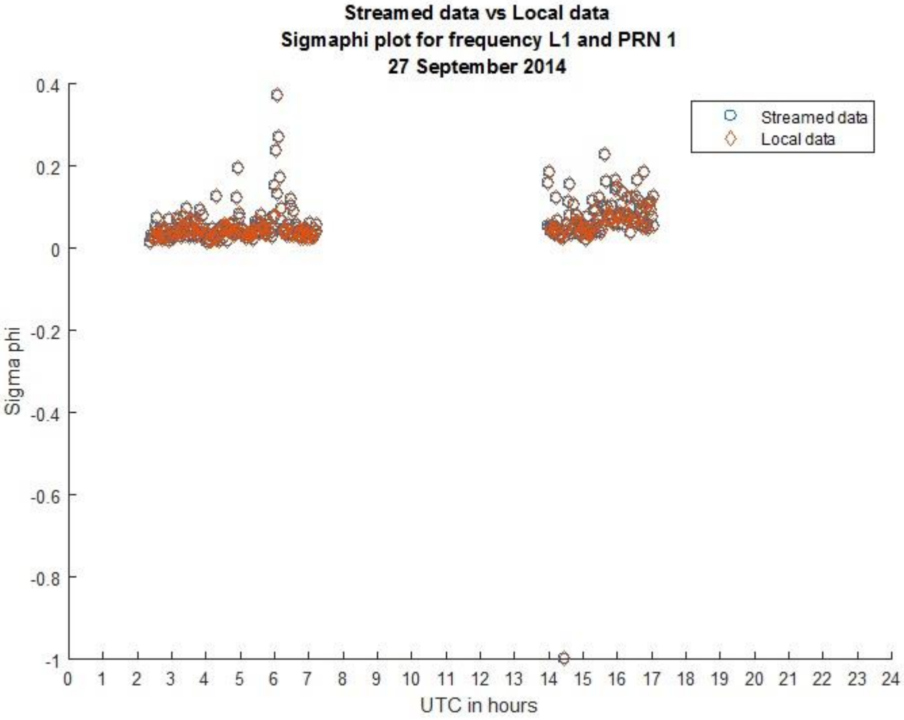

Figure 3.6. σ_ϕ values vs time from streamed and local data for L1 frequency, PRN 1 and RX 108 on September 27, 2014.

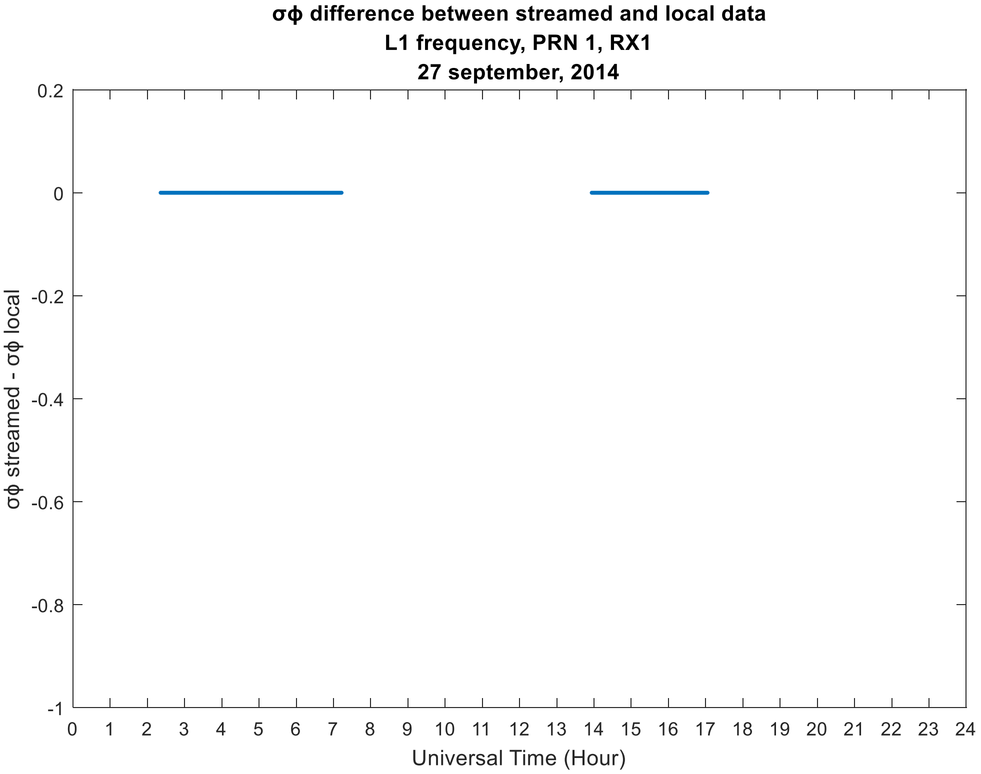

Figure 3.7. Difference of σ_ϕ values between streamed and local data vs time for L1 frequency, PRN 1 and RX 108 on September 27, 2014.

From Figures 3.4 and 3.6, the S4 value and the σ_ϕ value from the streamed and the local data at each timestamp are overlapping, respectively. Figures 3.5 and 3.7 show that the difference between the local and the streamed data for S4 and the σ_ϕ, respectively is zero. It can be concluded that the exact values of phase scintillation index and amplitude scintillation index are obtained from the streamed and the local data. Therefore, when both data sets exist on the server, either can be used for this research to detect the scintillation.

3.2 Automated Scintillation Detection

The previous contribution demonstrated that the local data and the streamed data are same, so the streamed data is used for the subsequent research. This is because the streamed data is directly retrieved from the IIT Apollo server and unpacked from binary format with one day latency, unlike transporting the local storages at Alaska to retrieve the local data. Therefore, the streamed data is more easily accessible than the local data on daily basis.

In this section, the process of detecting the phase scintillation and the amplitude scintillation for the GPS frequencies L1 and L2C will be explained. This constitutes the second contribution of this thesis.

The automated scintillation detection technique by [1] introduced in Chapter 2 is applied to detect the scintillations occurring on any given day. In the past, the detection technique was used to explore only L1 frequency phase scintillation [1] but for this research the same technique is modified to explore both phase and amplitude scintillations for both the GPS frequencies L1 and L2C. The scintillation files from the IIT server provides the required amplitude and phase scintillation indices. The flow chart in Figure 3.8 shows the steps involved in the automated scintillation detection routine.

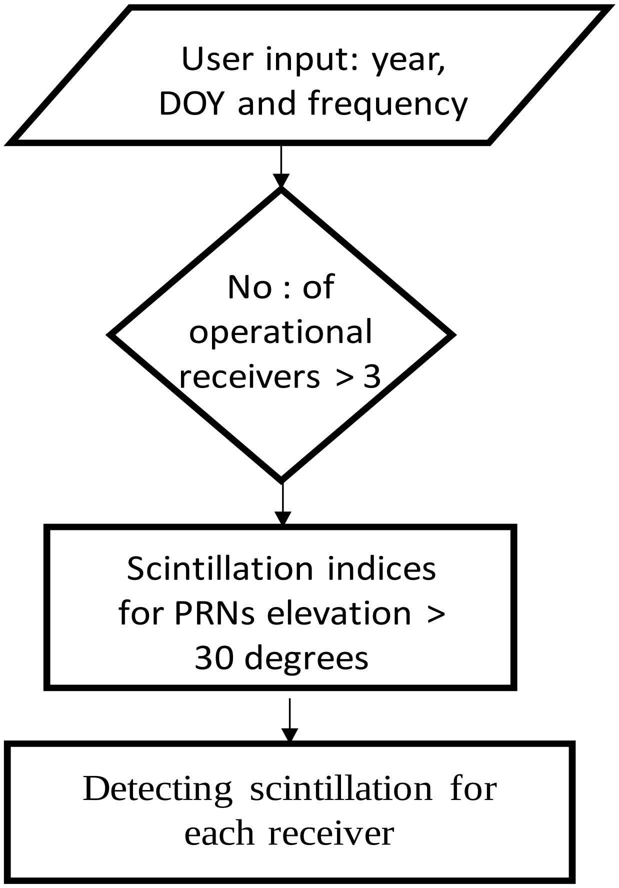

Figure 3.8. Summary of the steps in automated scintillation detection.

Previous work required multiple receivers to observe the scintillation [1] to avoid any false alarms. In this work, if the number of operational receivers on a day is fewer than four, then the automated scintillation detection routine will disregard that day. The scintillation must be detected by a minimum of four receivers, for it to be considered as real scintillation.

Multipath is a propagation phenomenon in which the signals from the transmitter hit the ground and then reach the receiver. This produces changes in the signals which alters the phase and the magnitude. These alterations due to multipath can be mistaken for pure scintillation but do not have an ionospheric source. The interaction of the multipath should be ignored while observing pure scintillation of signals from the transmitter. To minimize the chance of false alarms due to multipath, the scintillation indices of satellites below 30 degrees elevation are ignored.

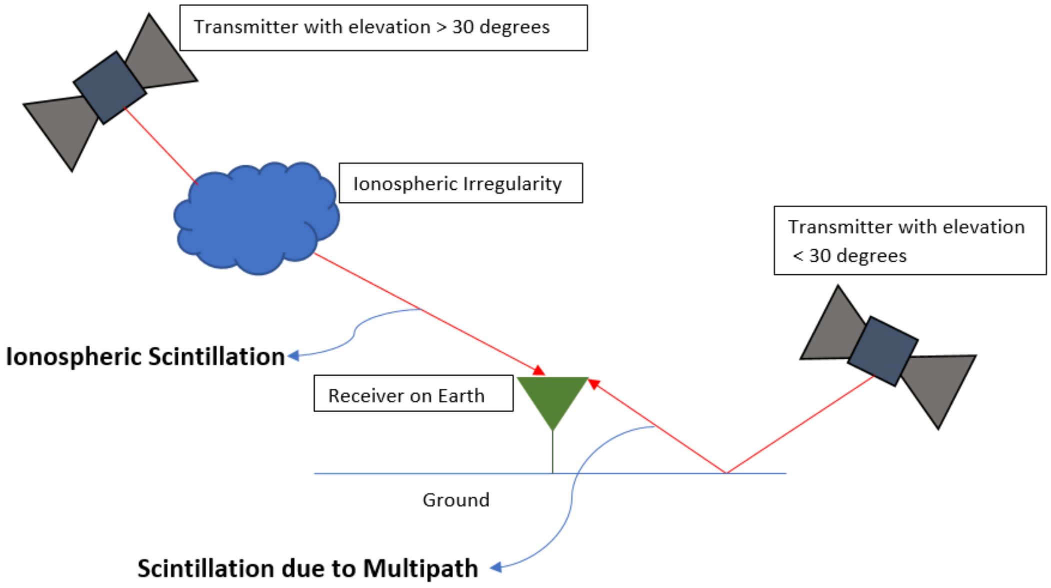

Figure 3.9. Multipath phenomenon.

Though scintillations happen on many days, it is significant to know on which days the highest or the lowest scintillation was observed and a measure called Weighted Scintillation Number (WSN) was adapted from [1].

$$\text{WSN} = \frac{N_{stat} * th_{stat} + N_{dyn} * th_{dyn}}{th_{stat} + th_{dyn}}$$

where,

th_{stat} – Static threshold. Set as 0.2 while detecting amplitude scintillations and 0.6 rad while detecting phase scintillations. This remains constant throughout the detection routine.

N_{stat} – Number of S4 or σ_ϕ measurements above the static threshold (th_{stat}).

th_{dyn} – Dynamic threshold. Takes the mean of all the S4 measurements for amplitude scintillation or σ_ϕ measurements for phase scintillation, throughout a day from all active receivers. It is different for different days.

N_{dyn} – Number of S4 or σ_ϕ measurements above the dynamic threshold (th_{dyn}).

The Weighted Scintillation Number (WSN) is a useful measure to quantify the strength of scintillation only if the scintillation has occurred on that day. In other words, though WSN is high, the scintillation may not necessarily occur on that day. WSN is just a number predominantly measuring the number of S4 or $\sigma\phi$ values exceeding the dynamic threshold (th_{dyn}) occurring on a day. If the dynamic threshold is below the static threshold, the WSN will be high but no scintillation could be detected if all the S4 or $\sigma\phi$

values lie below the static threshold. Depending on the WSN, the expected top ten days in the years 2014 and 2015 which are predicted to have high phase scintillation and amplitude scintillation are shown in Table 3.1 and 3.2, respectively.

Table 3.1. Top 10 days of 2014 for L1 and L2C frequency showing amplitude and phase scintillation. DOY: Day Of the Year.

2014										
L1 frequency						**L2C frequency**				
Amplitude Scintillation			**Phase scintillation**			**Amplitude Scintillation**			**Phase scintillation**	
DOY	**WSN**		**DOY**	**WSN**		**DOY**	**WSN**		**DOY**	**WSN**
196	360		120	1148		59	189		239	496
58	357		239	1134		281	174		293	482
193	343		50	1092		29	167		308	476
197	341		293	1075		57	166		314	467
189	339		282	1028		239	166		320	448
110	338		320	997		56	164		282	427
198	338		102	992		229	164		102	425
190	337		308	912		37	161		120	424
229	337		314	902		61	161		291	413
194	336		51	884		322	161		50	404

Table 3.2. Top 10 days of 2015 for L1 and L2C frequency showing amplitude and phase scintillation. DOY: Day Of the Year.

2015										
L1 frequency						**L2C frequency**				
Amplitude Scintillation			**Phase scintillation**			**Amplitude Scintillation**			**Phase scintillation**	
DOY	**WSN**		**DOY**	**WSN**		**DOY**	**WSN**		**DOY**	**WSN**
239	339		252	1309		302	192		239	655
130	338		239	1287		217	191		252	633
90	337		240	1243		303	191		280	632
290	337		280	1145		295	190		240	606
214	329		101	1140		218	189		311	577
208	328		76	1122		239	188		101	526
230	328		106	1053		133	187		307	525
251	328		311	987		225	186		263	514
281	328		54	986		90	184		106	506
117	325		132	977		213	184		76	500

The final stage of this automated scintillation detection routine is to find the time intervals during which the scintillation is happening on a day. The S4 or σ_ϕ measurements for an entire day at each operational receiver for each PRN with elevation above 30 degrees is considered. Between static and dynamic threshold, the one with higher value is set as the threshold for that day. For each PRN at each active receiver, the time intervals during which the S4 or σ_ϕ data points are "continuously" above the threshold constitute an amplitude or phase scintillation time interval, respectively. Three or more consecutive data points lying below the threshold, constitutes a scintillation discontinuity. Otherwise the interval is "continuous". The scintillating time that is common to a minimum of four operational receivers for each PRN is the scintillating time for a satellite on a day. The figure below reprinted from [1], explains the process of detecting the scintillation time and scintillation discontinuity.

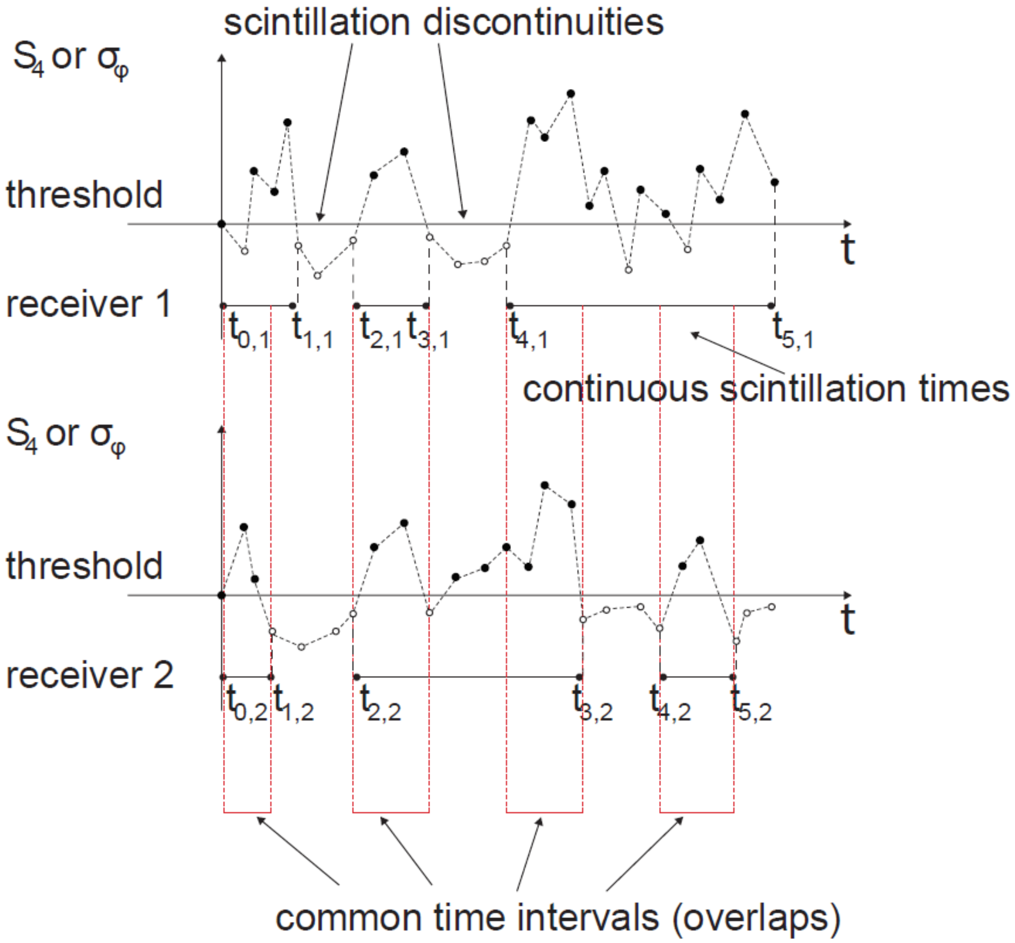

Figure 3.10. Illustration of the process of detecting the scintillating time interval for a satellite on a day. Image reprinted from [1].

The output of this automated scintillation detection routine for a given day and frequency is a list of PRN, scintillation time, total scintillation duration, average S4 or σ_{ϕ}. value, number of data points during that interval, number of operational receivers on that day. An example of this output for one of the top 10 days of 2014 with highest WSN for L2C phase is shown in Table 3.3.

Table 3.3 Output of phase scintillation detection routine for L2C frequency and DOY 239 and year 2014

PRN	Start hour	Start Min	End Hour	End Min	Total Duration (min)	Average (radians)	Data points	Operational receivers
30	13	18	13	35	17.46001745	2.004336113	45	5
24	18	31	18	42	11.55306548	1.897521963	17	5
30	12	59	13	15	16.35718027	1.671327292	48	5
6	9	31	9	46	14.95948652	1.577079512	43	5
30	14	22	14	32	10.00016838	1.533097215	24	5
24	18	9	18	19	10.00016201	1.523672437	24	5
9	9	32	9	50	18.02398542	1.281769803	52	5
17	16	22	16	33	10.5639937	1.256637061	20	5
7	12	50	13	11	20.98908668	1.237787506	63	5
1	6	12	6	29	16.35786809	1.23150432	45	5
6	8	40	8	57	17.45977957	1.083849465	48	5
17	18	56	19	9	12.46056961	1.068141502	37	5
7	14	25	14	37	11.66684864	1.011592834	29	5
12	18	2	18	18	15.56392718	1.008451242	40	5
31	7	19	7	31	12.23163435	1.005309649	37	5
31	8	35	8	47	11.86153578	1.005309649	37	5
24	16	38	16	57	19.43660147	0.961327352	53	5
15	16	46	17	6	20.00034615	0.92362824	40	5
24	17	16	17	26	10.60405064	0.907920277	30	5
5	13	43	14	1	17.7292995	0.889070721	54	5

CHAPTER 4

CLASSIFICATION OF SCINTILLATION

As introduced in Chapter 3, either phase or amplitude can be scintillating. The automated scintillation detection routine identifies these intervals. However, it is useful to check for intervals when both amplitude and phase are scintillating in case occurrence of both phase and amplitude scintillation is unique to one layer of the ionosphere. This chapter describes the process of identifying the common intervals between amplitude and phase scintillations, and classifies the scintillation into amplitude only, phase only or both.

4.1 Scintillation Event

Using the automated scintillation detection technique discussed in the previous chapter, the scintillation time periods for L1 and L2C frequency signals can be found for each PRN. A scintillation event is defined as the occurrence of scintillation during an interval for a given frequency and PRN. Each scintillation event can be classified based on the type of scintillation happening during that event time interval. Scintillation is classified into phase scintillation, amplitude scintillation, or both, depending on the fluctuation in the phase or the power or both, respectively, of the signal.

Figure 4.1 depicts scintillation events and explains the types of scintillation events i.e., only amplitude scintillation (Type 1) or only phase scintillation (Type 2) or both (Type 3).

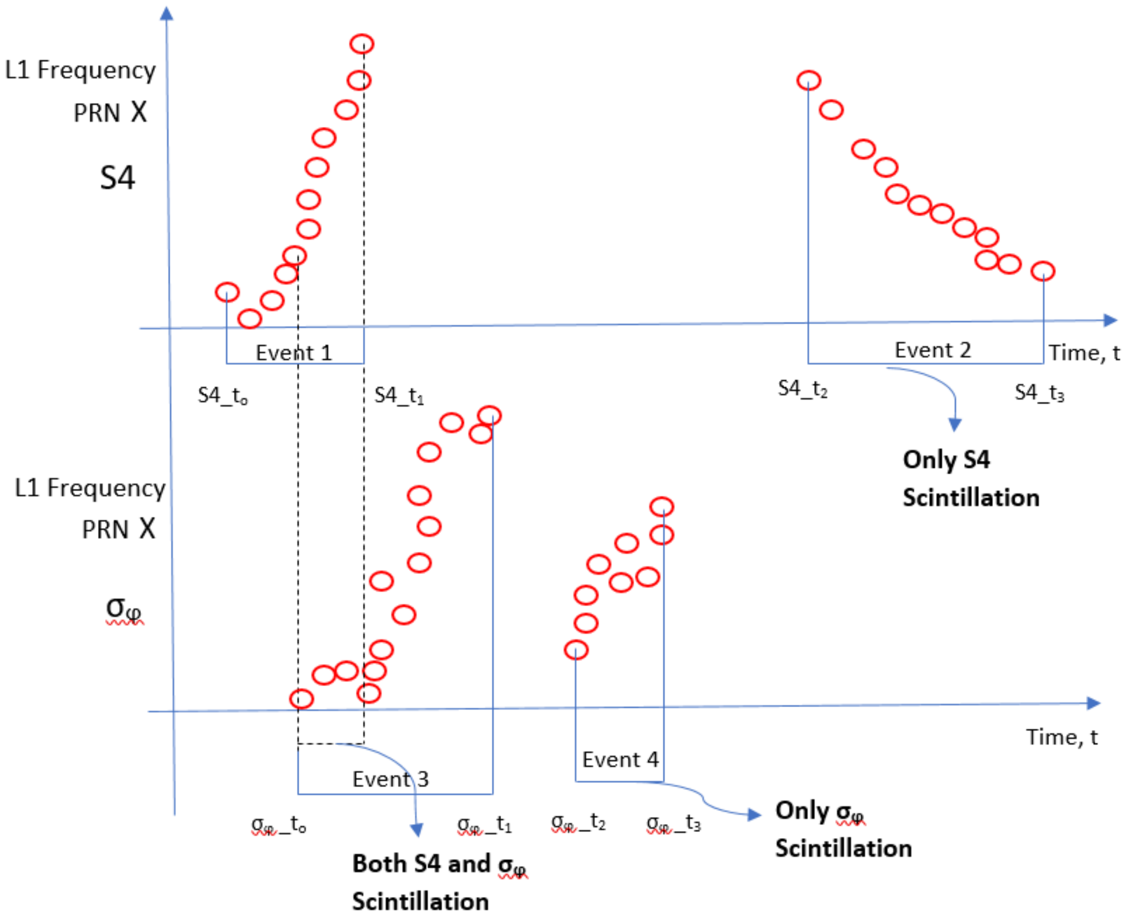

Figure 4.1. Pictorial representation of scintillation events and types

There are four scintillation events corresponding to PRN X and L1 frequency according to Figure 4.1. The automated scintillation detection gives these four scintillation events from PRN X and L1 frequency i.e., amplitude scintillations from time S4_t$_0$ to S4_t$_1$ (event 1) and from S4_t$_2$ to S4_t$_3$ (event 2) and phase scintillations from time σ_ϕ_t$_0$ to σ_ϕ _t$_1$ (event 3) and also from σ_ϕ _t$_2$ to σ_ϕ _t$_3$ (event 4). The following table summarizes these four events.

Table 4.1. Example of events summary from automated scintillation detection routine [1].

Event No	Start time	End time
1	$S4\_t_0$	$S4\_t_1$
2	$S4\_t_2$	$S4\_t_3$
3	$\sigma_\phi\ \_t_0$	$\sigma_\phi\ \_t_1$
4	$\sigma_\phi\ \_t_2$	$\sigma_\phi\ \_t_3$

The types of scintillation events are only amplitude, only phase and both. Event 2 depicts only amplitude scintillation as there is no phase scintillation detected during the period from $S4\_t_2$ to $S4\_t_3$. Similarly, event 4 depicts only phase scintillation, as no amplitude scintillation is detected by the scintillation detection routine for the scintillating period $\sigma_\phi\ \_t_2$ to $\sigma_\phi\ \_t_3$.

Unlike events 2 and 4, events 1 and 3 have common scintillating time during which both amplitude and phase scintillations have been detected. The time from $\sigma_\phi\ \_t_0$ to $S4\_t_1$, shows both phase and amplitude scintillation. This leads to a new subset event from the events 1 and 3 depicting a third class of scintillation i.e., both S4 and σ_ϕ scintillation.

Table 4.2. Classification of the detected four scintillation events from figure 4.1 based on the scintillation types.

Event No	Start time	End time	Scintillation Type
1	$S4\_t_0$	$\sigma_\phi\ \_t_0$	Only Amplitude
2	$S4\_t_2$	$S4\_t_3$	Only Amplitude
3	$S4\_t_1$	$\sigma_\phi\ \_t_1$	Only Phase
4	$\sigma_\phi\ \_t_2$	$\sigma_\phi\ \_t_3$	Only Phase
5	$\sigma_\phi\ \_t_0$	$S4\_t_1$	Both

Another scenario in which a possibly common interval between both scintillations can be identified. Suppose event 1 in figure 4.1 was phase scintillation for the same event 1 interval as mentioned in table 4.1, and that event 3 in figure 4.1 was amplitude scintillation for the same event 3 interval as mentioned in table 4.1. The common interval between both the scintillations would remain unchanged. In other words, the common interval between amplitude and phase scintillation is identified irrespective of whether S4 or σ_ϕ begins to scintillate first. Therefore, the maximum start time between S4_t_0 and σ_ϕ _t_0 is considered the new start time for the subset event and the minimum end time between S4_t_1 and σ_ϕ _t_1 is considered as the new end time for the same.

The definition of a scintillation event can be modified to continuous scintillation during an interval corresponding to one type of scintillation and one PRN and one frequency. Therefore, the initial four scintillation events are broken down to five different scintillation events after the classification based on the type of scintillation.

4.2 Scintillation classification algorithm

The logic to identify events such as event 5 in table 4.2, has been implemented. The flow chart below describes the process of detecting the type of scintillation occurring during each scintillating time.

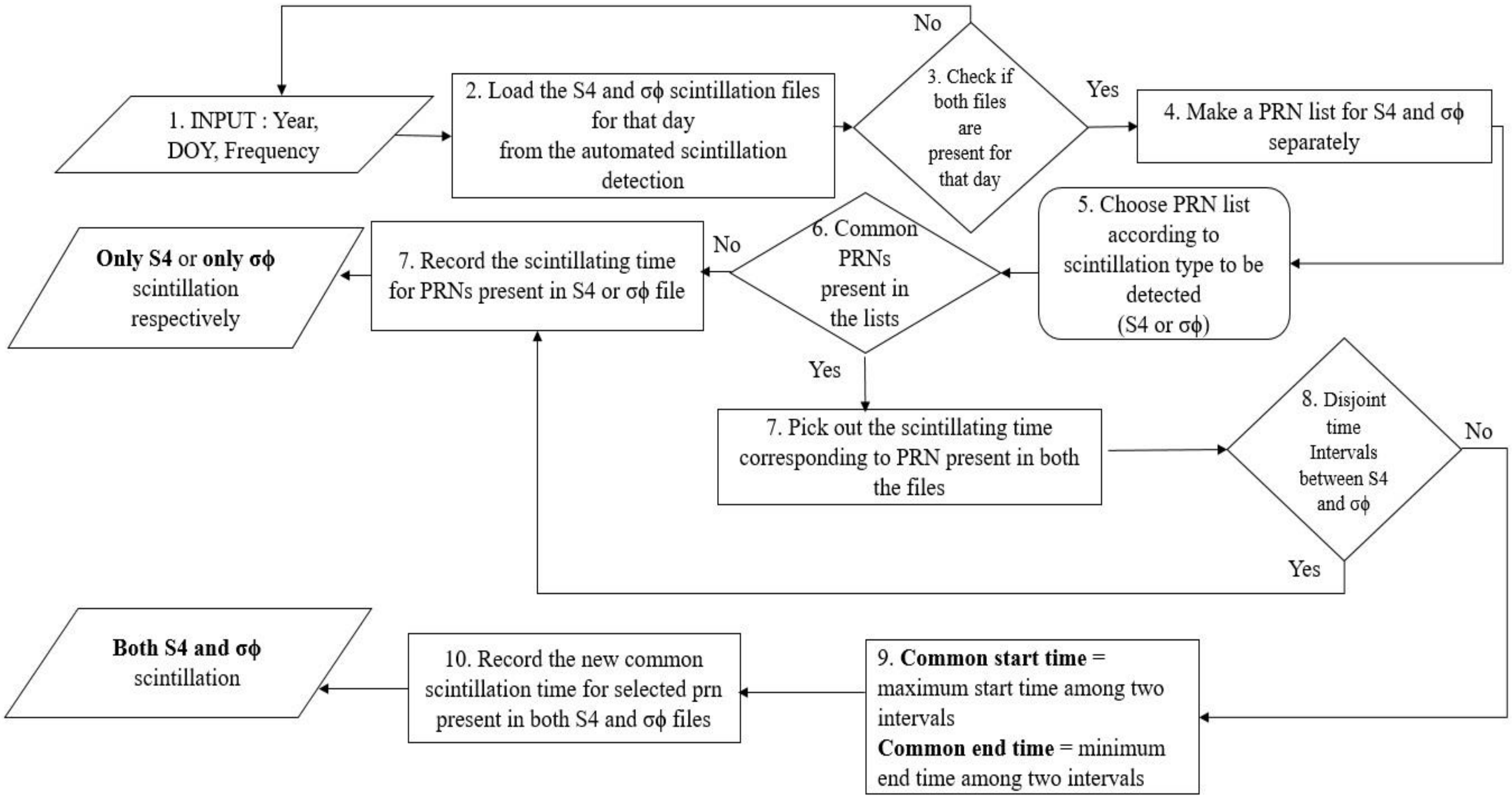

Figure 4.2. Algorithm for scintillation classification.

Step 1: The GPS frequency, year and day of the year for which the scintillation events are to be categorized are entered by a user.

Step 2: For a given date and frequency, the amplitude scintillation file and the phase scintillation file obtained from the automated scintillation detection, are loaded.

Step 3: If both the files are not present for the day given by the user, then no scintillation has occurred on that day. If either of the files is present, then the algorithm continues.

Step 4: A list of unique PRNs present in each file is created separately and labeled as S4_PRN list and σϕ_PRN list.

Step 5: To identify only amplitude or only phase scintillation events, the S4_PRN list or σϕ_PRN list is selected respectively. To find scintillation events when both the amplitude and the phase scintillations had occurred, consider both the PRN lists.

The above described steps 1 – 5 are common and fundamental to categorize any scintillation event into phase-only, amplitude-only or both. The following three subsections 4.2.1 – 4.2.3 explains the next steps involved in determining each of the scintillation category.

4.2.1 Only Amplitude Scintillation. To determine the scintillation events when there is only amplitude scintillation occurring, the S4_PRN list is considered first. The PRNs which are present only in the S4_PRN list and not in the σϕ_PRN list implies that only amplitude scintillation has occurred for these PRN on that day considered. The scintillation time intervals corresponding to the unique PRNs and its frequency gives only amplitude scintillation event of the day.

4.2.2 Only Phase Scintillation. As with the process of detecting the amplitude-only scintillation events, the phase-only scintillation events are also identified. To determine this, the σϕ_PRN list is considered and the PRNs which are unique to this list and not present in the S4_PRN list implies that the scintillation events associated with these PRNs are only phase scintillation events. The scintillation time corresponding to these unique PRNs and their frequency gives only phase scintillation events for that day considered. The following is an example of only phase scintillation event identified through this algorithm.

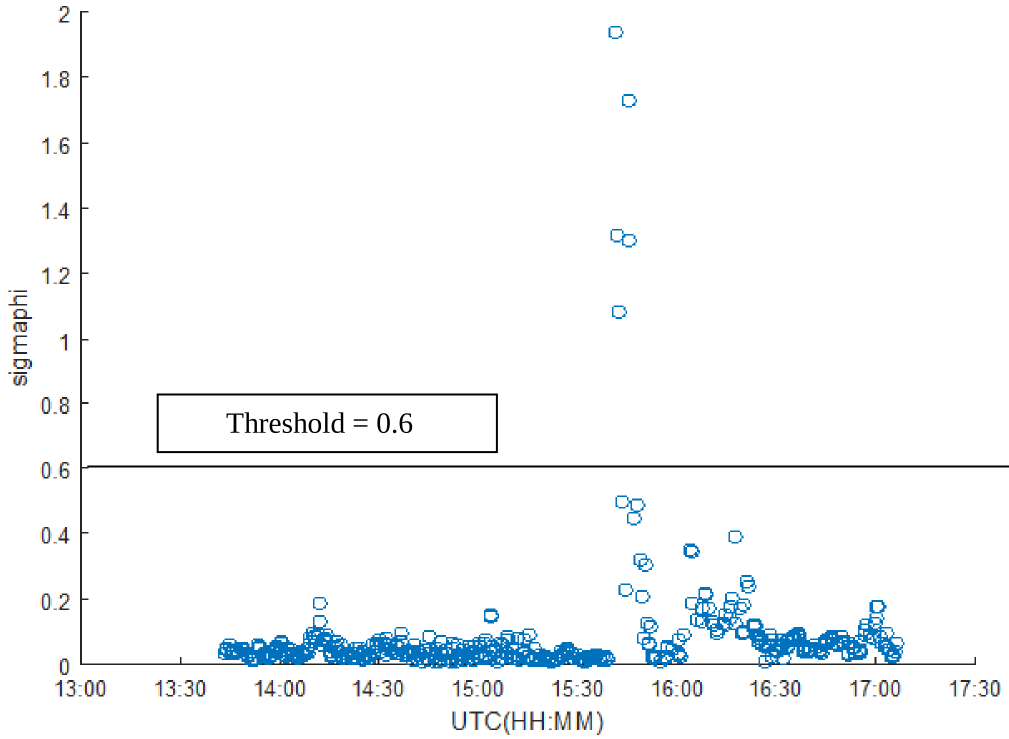

Figure 4.3. Plot of σ_ϕ values from PRN 27 and frequency L2C on February 27, 2014 with threshold set at 0.6 rad.

The table below gives the time during which the scintillation occurred.

Table 4.3 Phase scintillation event from automated scintillation detection technique for PRN 27 and L2C frequency.

PRN	Start HH	Start MM	End HH	End MM
27	15	42	15	55

No amplitude scintillation was detected on the same day from same PRN 27 and frequency L2C as all the S4 data points were below the threshold set at 0.2. It can be witnessed from the figure below.

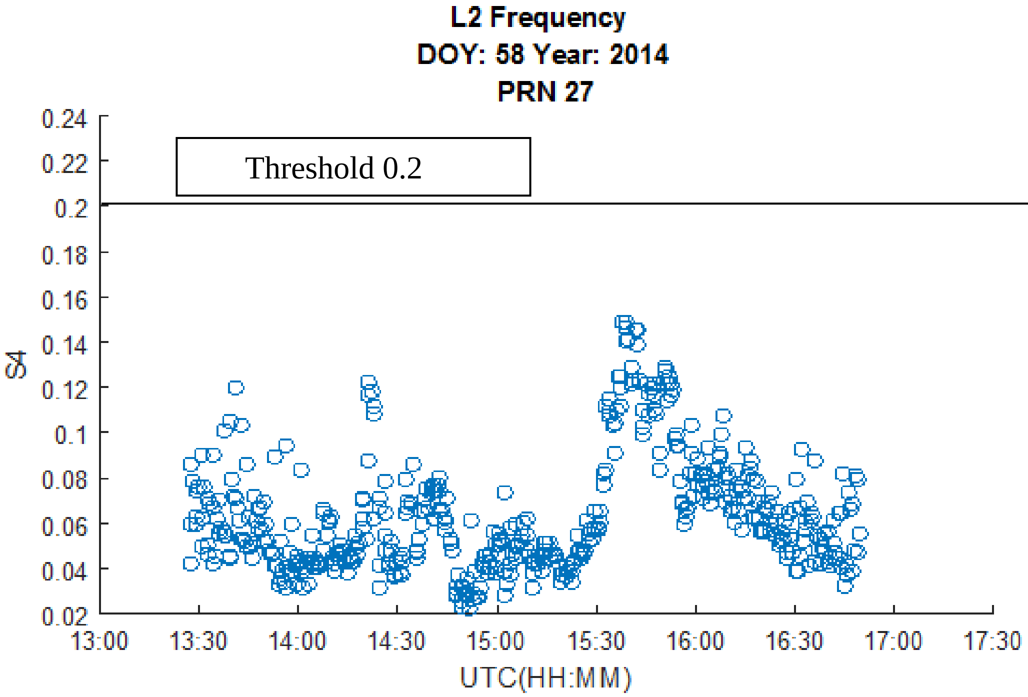

Figure 4.4. Plot of S4 values from PRN 27 and frequency L2C on February 27, 2014 with threshold set at 0.2.

Since PRN 27 shows only phase scintillation, it was recorded as an only phase scintillation event by the scintillation classification algorithm.

4.2.3 Amplitude and Phase scintillation. The PRNs common to both the amplitude scintillation events and the phase scintillation events are considered for this last scintillation type. The existence of overlapping time intervals between these two scintillation events from the automated scintillation detection routine is checked. If there is an overlapping time interval, then the duration common to both is considered to belong to the both amplitude and phase scintillation type. If there is no overlapping time interval, the scintillation time intervals during which amplitude and phase scintillations are occurring are disjoint. In that case, no event of both amplitude and phase scintillations is detected for that day. The amplitude scintillation and the phase scintillation from same PRN and same frequency on a day but different time intervals will result in the only-amplitude scintillation event and only-phase scintillation event respectively. The following is a case where both amplitude and phase scintillation has been detected by this algorithm.

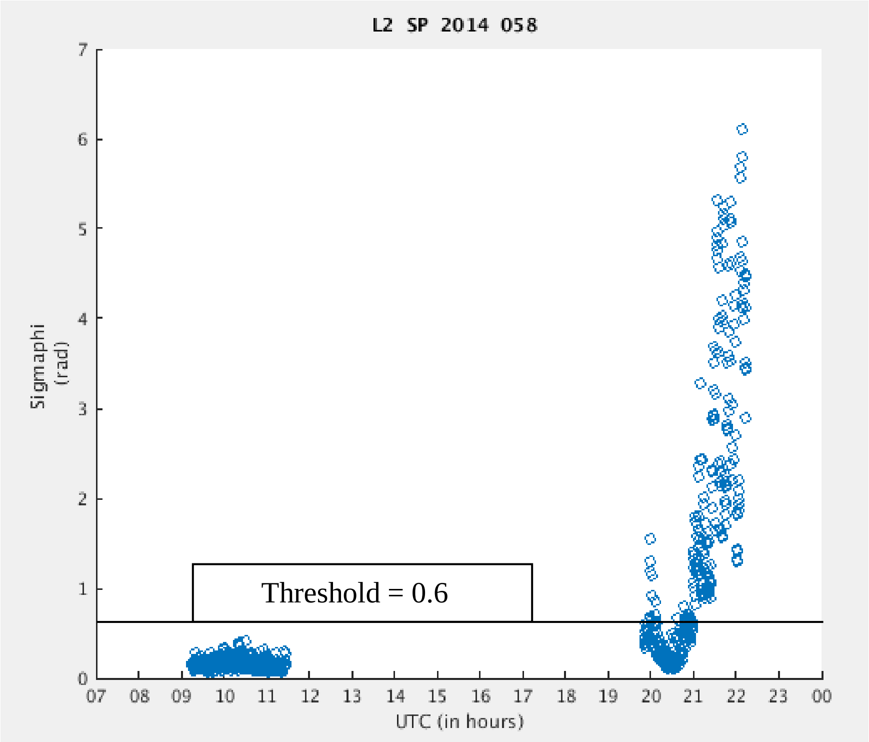

Figure 4.5. Plot of σ_ϕ values from PRN 30 and frequency L2C on February 27, 2014 with threshold set at 0.6 rad.

There is phase scintillation occurring as there are σ_ϕ continuous data points present above the threshold set at 0.6 radians. The table below shows the duration of phase scintillation for PRN 30, L2C frequency on February 27, 2014.

Table 4.4 Phase scintillation event from automated scintillation detection technique for PRN 30 and L2C frequency on February 27, 2014.

PRN	Start HH	Start MM	End HH	End MM
30	20	57	22	13

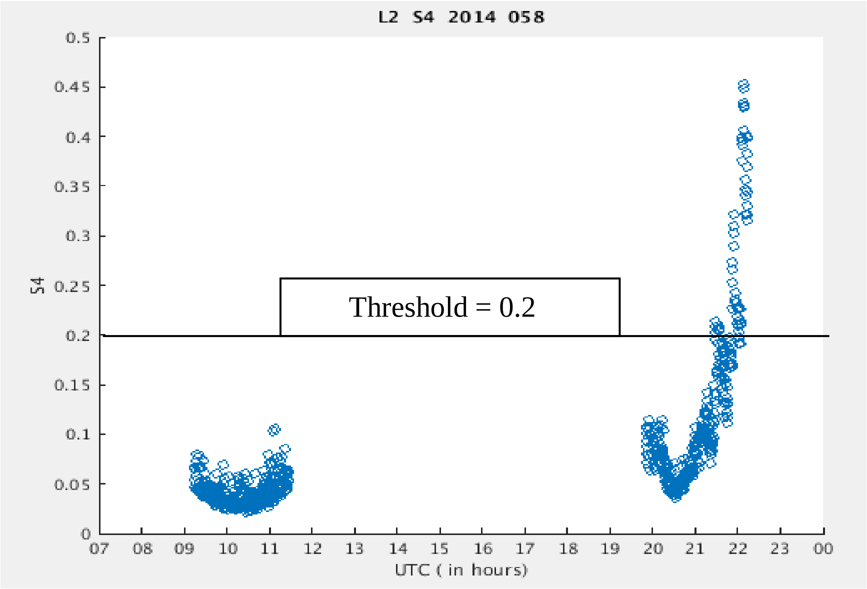

Figure 4.6. Plot of S4 values from PRN 30 and frequency L2C on February 27, 2014 with threshold set at 0.2.

Since there are continuous S4 data points above the threshold set at 0.2, there is amplitude scintillation occurring on the day February 27, 2014 from PRN 30 and L2C frequency. The table below shows the duration of amplitude scintillation for PRN 30, L2C frequency on February 27, 2014.

Table 4.5 Amplitude scintillation event from automated scintillation detection technique for PRN 30 and L2C frequency on February 27, 2014.

PRN	Start HH	Start MM	End HH	End MM
30	22	2	22	13

There is a common time interval between the amplitude scintillation and the phase scintillation. This common time is considered for the third scintillation type i.e., both amplitude and phase scintillation. The following is the result from the scintillation type detection algorithm, showing an event when there is both amplitude and phase scintillations occurring.

Table 4.6 Amplitude and Phase scintillation event detected by the scintillation type detection algorithm.

PRN	Start HH	Start MM	End HH	End MM
30	22	2	22	13

CHAPTER 5

E AND F LAYER IRREGULARITIES

In this chapter, the processes to identify whether the E or F region is causing the observed scintillation are discussed. The two scintillation events from research done in the past and mentioned in Chapter 2 are,

i) phase scintillation in F region on December 8, 2013 at 3:45-4:15 UT [2] and

ii) phase scintillation in E region on October 7, 2015 [3].

These case studies on scintillation events are used to develop a general algorithm to identify the ionospheric region irregularities associated with different scintillation events. The following sections describe the methods of ionospheric region detection based on PFISR data and all sky camera images.

5.1 Poker Flat Incoherent Scatter Radar

As discussed before, the incoherent scatter radar at Poker Flat Research Range, Alaska, provides properties of ionospheric state such as, electron temperature, ion temperature, electron density, altitude at which these properties were observed, range, etc. The Madrigal database at [15], is a platform to access all these data for any day.

Out of all the parameters that are available, the electron density is essential for this research. Since scintillation is due to diffraction of GPS signal caused by variation of density in the plasma i.e., ionospheric irregularities, we assume the electron density is directly proportional to the irregularities. In other words, higher electron density can give rise to higher variations in density, in the form of irregularities. Based on the electron density Ne, an algorithm is developed to determine the altitude at which a scintillation event is occurring.

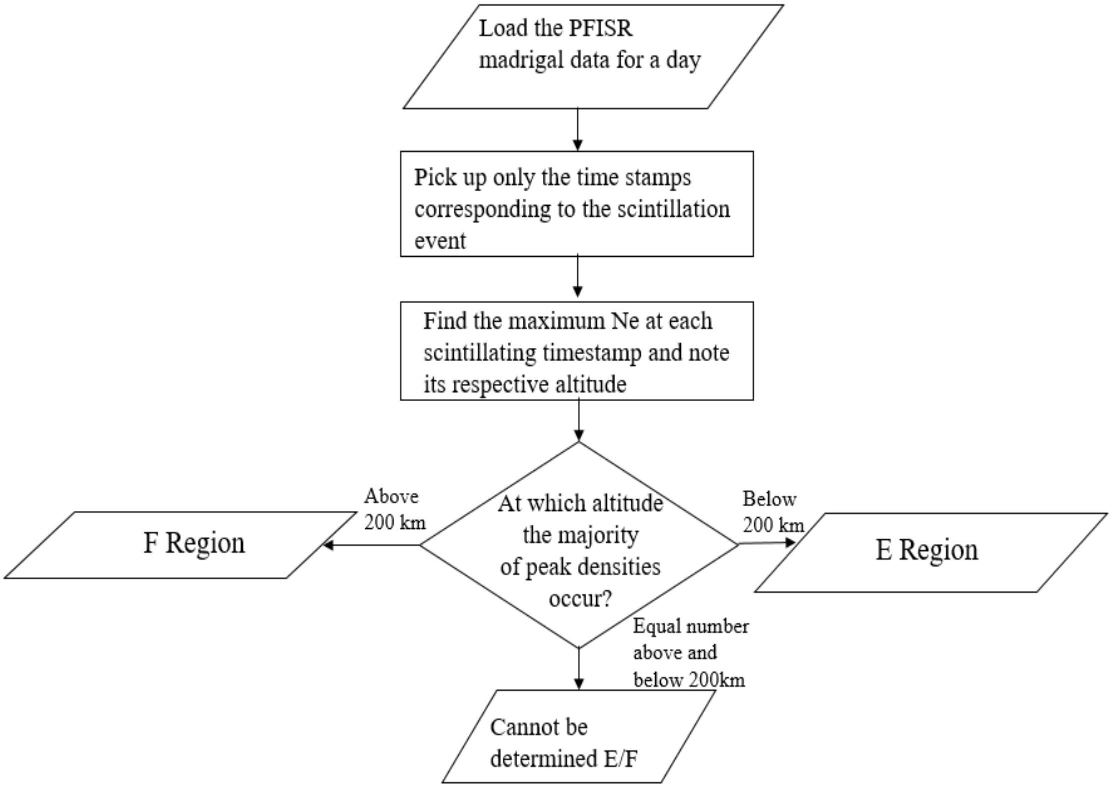

Figure 5.1. An algorithm to identify the E or F region causing scintillation based on Ne.

The above flow chart describes the steps involved in identifying the ionospheric irregularities responsible for a scintillation event. The PFISR density data for the day on which the scintillation is happening is downloaded from the Madrigal. Parameters such as Universal Time hour, minute, second, day of the year, month, year, day, electron density, altitude, beam elevation and beam azimuth are needed. It can be noticed from the PFISR data that at each timestamp, different altitudes and Ne are observed at various combinations of beam azimuth and beam elevation. The electron densities and the altitudes measured for the radar beam whose azimuth and elevation are near the scintillating PRN’s azimuth and elevation are considered for this algorithm. From the PFISR data file, only the Ne and the altitudes corresponding to the scintillating period and the PRN elevation and PRN azimuth are picked out. We find the altitude at which the maximum Ne is occurring for each scintillating time stamp. These peak heights are compared to a threshold of 200 km. The 200 km is set as a threshold because this altitude acts as an approximate boundary between the E and F layers. If the maximum number of data points are lying above 200 km altitude during that scintillation event, then the scintillation is determined to be occurring in the F region. If the maximum number of data points are lying below 200 km altitude during that scintillation event, then the scintillation is determined to be occurring in the E region. If the number of data points are equal above and below 200 km altitude then the region causing that scintillation event cannot be determined using PFISR data.

The F and E region scintillation events mentioned in Chapter 2 are taken as examples to demonstrate this algorithm. First, December 8, 2013 on which the F- region caused phase scintillation is considered.

Table 5.1 Scintillation events on 8th December 2013.

PRN	**Start HH**	**Start MM**	**End HH**	**End MM**	**Type**	**Frequency**
23	3	43	4	17	Phase	L1
10	3	50	4	41	Phase	L1

The above two scintillation events obtained from the automated scintillation detection routine in Chapter 3 exactly matches with the scintillating time observed on this day in previous research which is to be expected since the same automated scintillation detection routine was used for both [2]. To find the region at which this scintillation is occurring, the altitude of maximum Ne at each timestamp during the scintillating interval is plotted. The figure below shows the altitude versus scintillating time for the scintillating PRN 23.

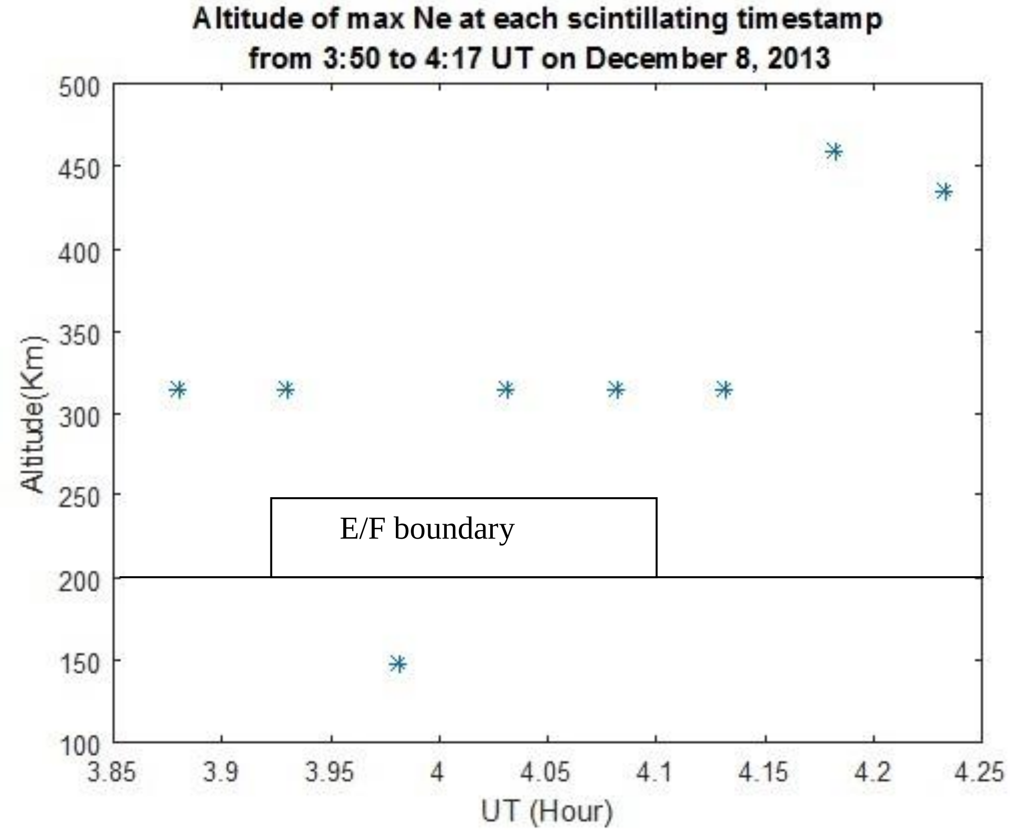

Figure 5.2. Altitude of maximum Ne, for PFISR beam of azimuth 14.4 degrees and elevation of 90 degrees (closest to PRN's azimuth and elevation), at each scintillating period on December 8, 2013.

It can be seen from the above figure that the majority of maximum Ne are occurring above 200 km. Almost at every timestamp the maximum Ne is occurring above

200 km. For this reason, concluding as prior studies showed [2], it is a F- region scintillation event.

The second event mentioned in the beginning of this chapter is E-region phase scintillation on October 7, 2015. The automated scintillation detection routine detected two phase scintillation events on the same date and its scintillating time is comparable to the scintillation time observed in the previous research [3].

Table 5.2 Scintillation events detected on 7th October 2015.

PRN	Start HH	Start MM	End HH	End MM	Type	Frequency
3	6	02	6	20	Phase	L1
6	6	03	6	45	Phase	L1

The altitude corresponding to maximum Ne at each scintillating time from 06:03 UT to 06:20 UT is plotted, shown in Figure 5.3.

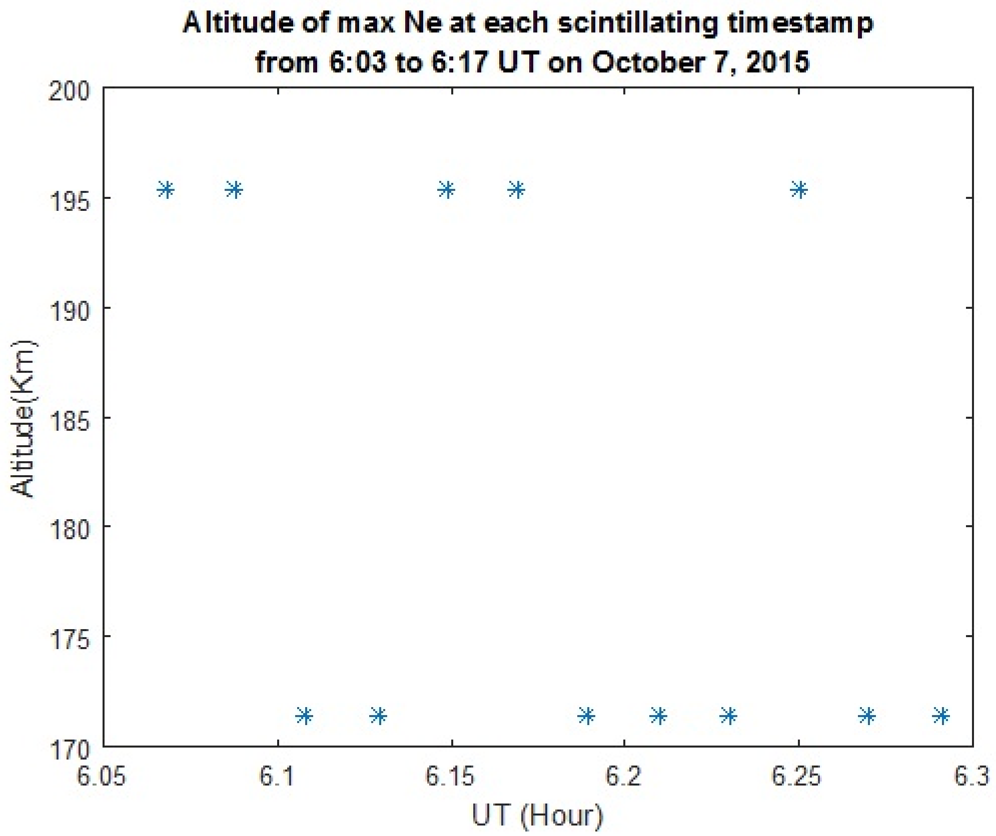

Figure 5.3. Altitude of maximum Ne at each scintillating period on October 7, 2015

From the figure, at each scintillating time stamp the maximum Ne is occurring below 200 km. Therefore, this scintillation event is an E – region scintillation and agrees with the result from prior research [3].

5.2 All Sky Camera

As mentioned in Chapter 2, the all sky camera located at Poker Flat Research Range, Alaska, captures the auroras appearing in the sky during night. This all sky camera is considered as another resource to determine the altitude at which the scintillation is occurring. It is in the same vicinity as PFISR and also a reliable resource to compare with the results obtained from the algorithm described in the previous section.

The auroral images throughout the night are available in the FITS file format from [16]. The red auroral brightness image and the green auroral brightness image are readily available for timestamps throughout a night. Generally, the red auroral brightness (630.0nm) is linked with F region ionospheric activity, and the green auroral brightness (557.7 nm) indicates E region activity. In this work, we assume that the region of activity is the region in which irregularities are likelier to be occurring.

Here, the same scintillation events in Table 5.1 and Table 5.2 for determining the altitude based on PFISR data is used to identify the altitude based on the red and green brightness captured during those scintillation events. On December 8, 2013, the scintillation events listed in Table 5.1 is considered again in this section. The scintillation exactly at 04:00 UT is observed from PRN 23 and PRN 10 . The red auroral brightness and the green auroral brightness at 04:00 UT on this day is plotted. A sky plot of the scintillating PRNs 10 and 23 are marked on top of the auroral image in Figure 5.4.

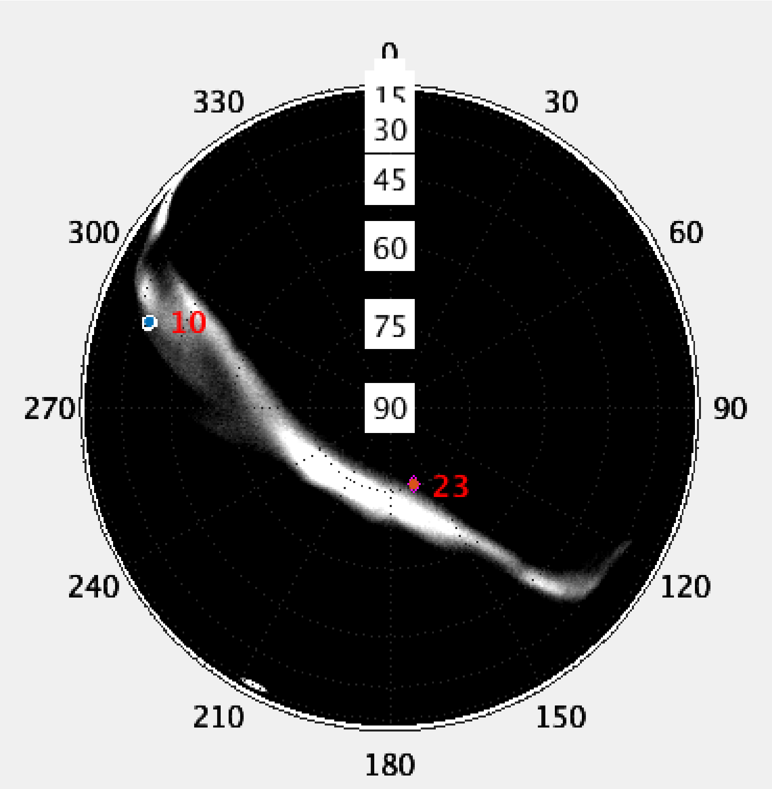

Figure 5.4. Red aurora on December 8, 2013 at 04:00 UT with PRN 10 and PRN 23 scintillating during the same time.

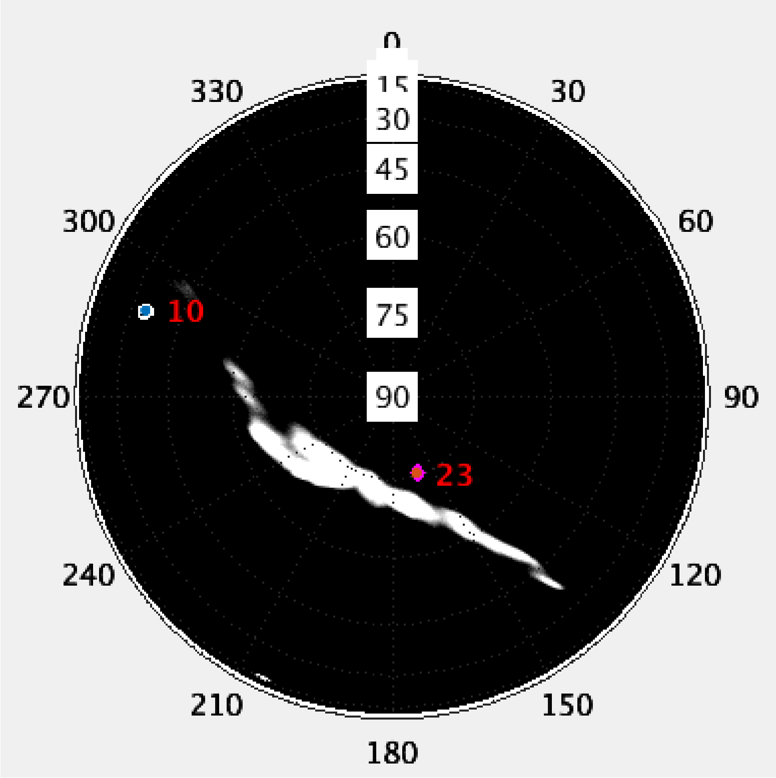

Figure 5.5. Green aurora on December 8, 2013 at 04:00 UT with PRN 10 and PRN 23 scintillating during the same time.

Though both the auroral arcs red and green are present during the scintillation time, the PRNs 10 and 23 are spotted along the red brightness arc. Whereas the same PRNs are spotted outside the green auroral region during that scintillation event. This confirms that the scintillation has occurred in the F region on December 8, 2013 at 04:00 UT. The red brightness and the green brightness pixels just at the location of the scintillating PRNs 23 and 10 are plotted against time for the whole scintillating interval from 3:50 to 4:17 UT. Figure 5.6 shows the red brightness and green brightness pixels at the location of scintillating PRN 10 against scintillating time at an interval of 5 minutes, for simplicity.

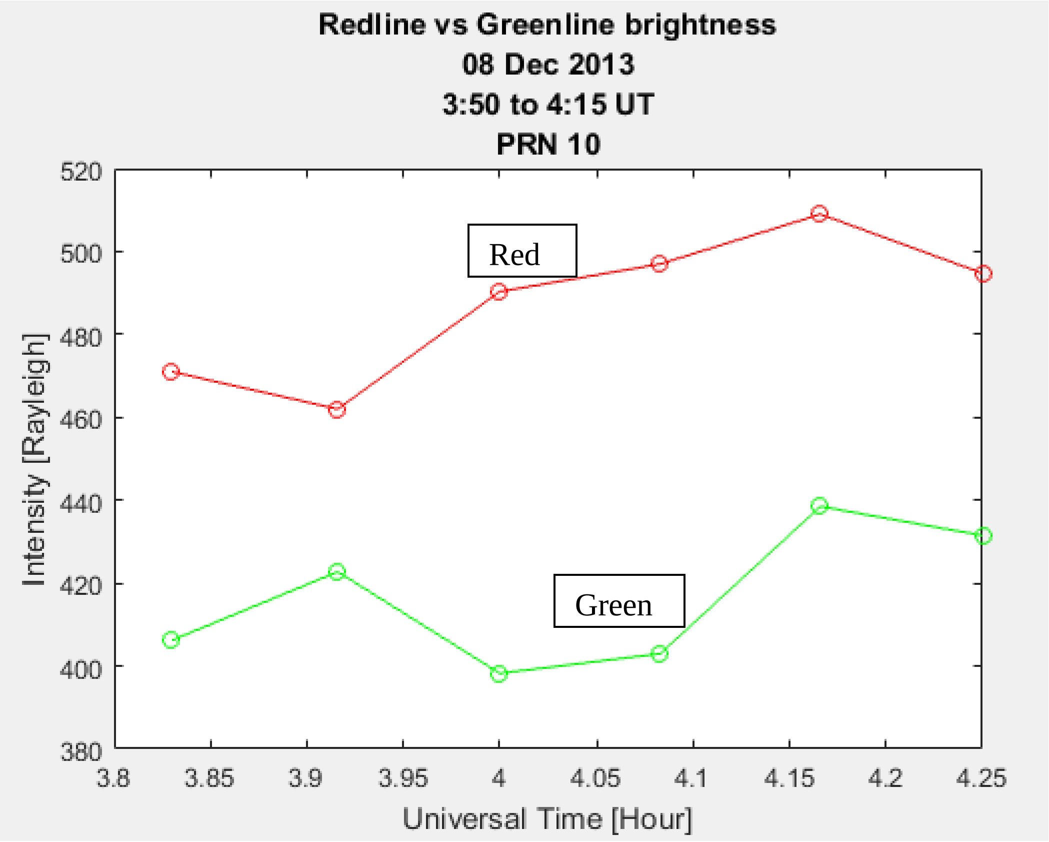

Figure 5.6 Red line and green line brightness captured during the 8th December 2013 scintillation event.

The red line is found to be brighter than the green line from 3:50 to 4:17 UT. This once again corroborates that it is F-region scintillation.

Similarly, for 7th October 2015, the same scintillation events listed in Table 5.2 in are considered here. The red line auroral arc and the green line auroral arc are plotted with the sky plot of PRN 3 and PRN 6 on top of it in Figure 5.7 and Figure 5.8, respectively.

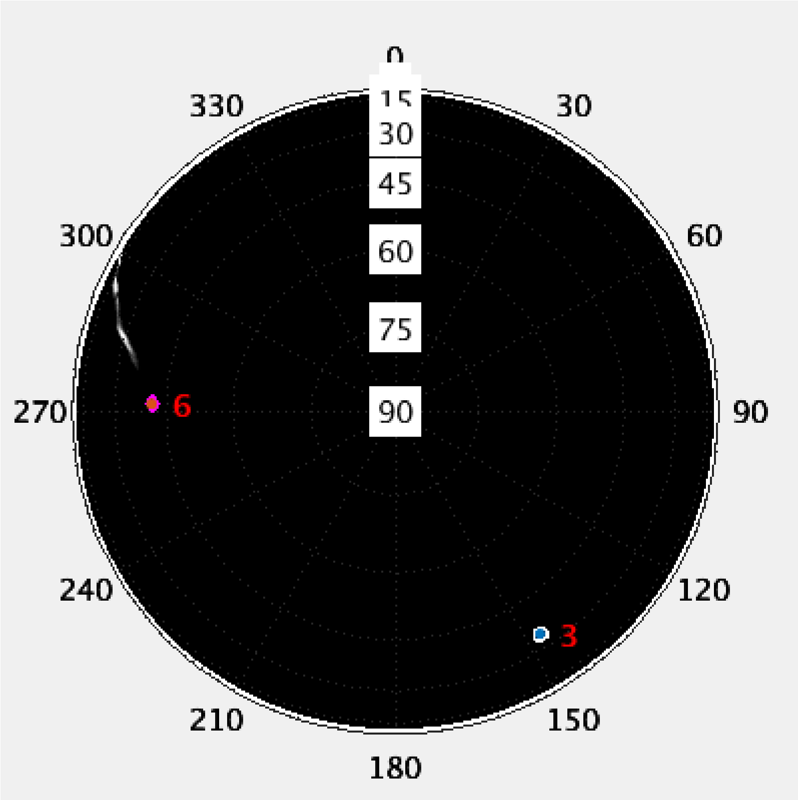

Figure 5.7. Red aurora on October 7, 2015 at 6:17 UT with PRN 3 and PRN 6 scintillating during the same time.

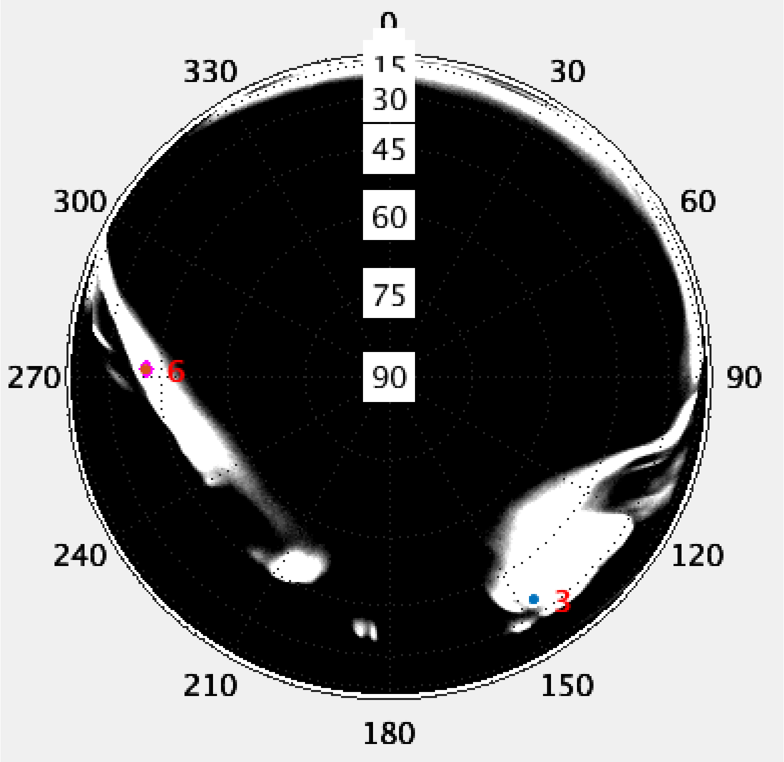

Figure 5.8. Green aurora on October 7, 2015 at 6:17 UT with PRN 3 and PRN 6 scintillating during the same time.

PRNs 3 and 6 are found to lie on the green line brightness. A very strong green line is captured compared to the red line. There is hardly an occurrence of red line brightness on this day at this time. Since the scintillating PRNs are clearly on the green line, it can be concluded that these events are related to E region scintillation.

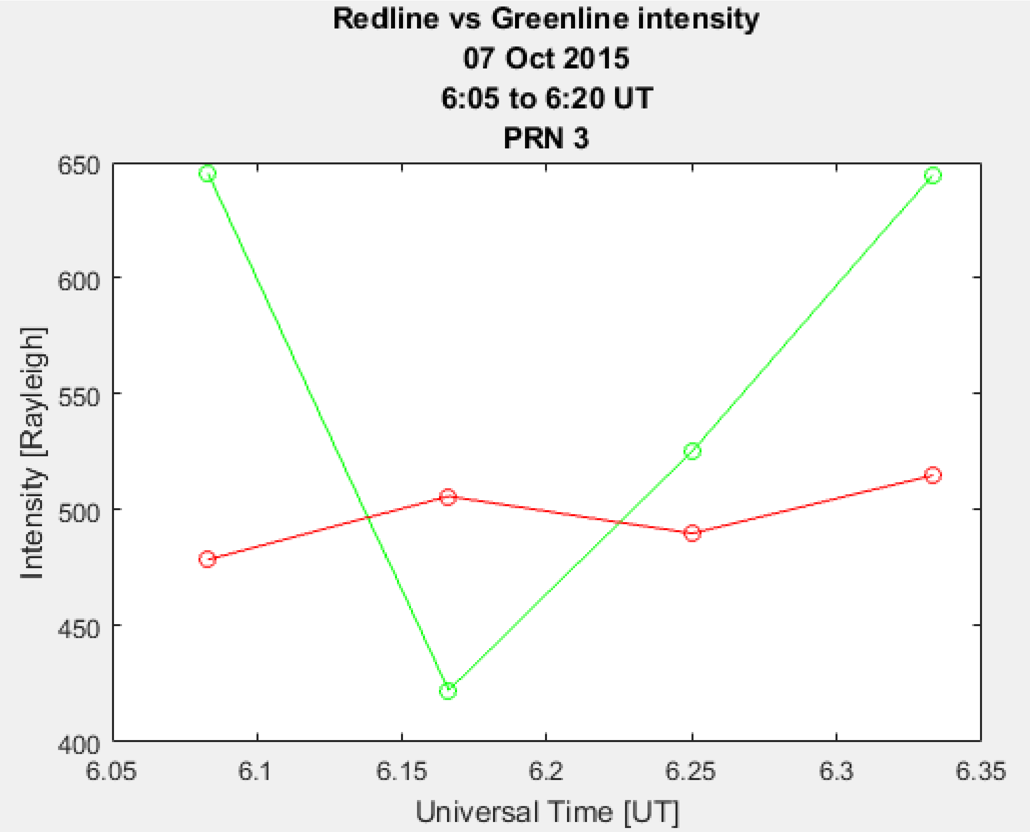

Figure 5.9. Red line and green line brightness vs time captured during the 7th October 2015 scintillation event.

The above figure compares the redline and the green line brightness for the scintillation events on October 7, 2015. The green line brightness is higher than the redline brightness during that complete scintillation event. Therefore, it is an E-region scintillation.

Both PFISR and All Sky Camera (ASC) processes to identify the irregularity region causing a scintillation event, have produced the same results. Therefore, the algorithm based on PFISR data is working reasonably as its results matches with the ASC results. PFISR and ASC are two independent resources to identify the irregularities. Note that PFISR does not necessarily run in the same mode or every night. Meanwhile, ASC data quality is reduced if there is significant cloud cover. So in cases where data are not available or a determination cannot be made from one instrument, the other may be used for assessment. The events discussed in this chapter are summarized in the following table.

Table 5.3 Summary of the scintillation events detected on 8th December 2013 and 7th October 2015 and their corresponding E/F irregularities causing these events.

Event	Date	PRN	Start HH	Start MM	End HH	End MM	Type	Frequency	Region
1	12-08-2013	23	3	43	4	17	phase	L1	F
2	12-08-2013	10	3	50	4	41	phase	L1	F
3	10-07-2015	3	6	2	6	20	phase	L1	E
4	10-07-2015	6	6	3	6	45	phase	L1	E

CHAPTER 6

CONCLUSION

This chapter summarizes the contributions of this thesis and its results. Here, also the application of each contribution to surveying scintillation events in 2014 and 2015 will be discussed. And finally, the future research which will be done based on the results obtained from this thesis will be explained.

6.1 Summary

The first contribution of this thesis, is to check whether the two sources of datasets i.e., streamed and local, obtained from the SAGA are the same or have variations in the data sets. The S4 or σ_ϕ values between the start time and end time common to both the data sets from one receiver and one frequency were plotted for a day. The result showed that when they both exists the streamed and the local data sets contain exactly same amount of data, given that the common start and end time is considered from both the data sets. Also, the difference of time stamp between both the data sets is zero and the difference of S4 or σ_ϕ values at each time stamp between the local and streamed data sets is zero. From this, it is concluded that when both the local and streamed data exists for a receiver, they are equivalent, and any one data set can be used for the research purpose. In this work, the streamed data are used.

The second contribution of this thesis is extending the automated scintillation detection technique, explained in Chapter 2, to explore the amplitude and phase scintillations occurring on L1 and L2C frequencies for all the days of the years 2014 and

2015 for which streamed data exist. The detection routine successfully explored many L1 and L2C frequencies phase scintillations and a few amplitude scintillations in the year 2014 and 2015. The top ten days of 2014 and 2015 sorted by decreasing Weighted Scintillation Number (WSN) of phase are tabulated below.

Table 6.1 Top 10 days of 2014 and 2015 of streamed data with highest WSN.

Phase Scintillation							
2014				**2015**			
L1 Frequency		**L2C Frequency**		**L1 Frequency**		**L2C Frequency**	
DOY	**WSN**	**DOY**	**WSN**	**DOY**	**WSN**	**DOY**	**WSN**
120	1148	239	496	252	1309	239	655
239	1134	293	482	239	1287	252	633
50	1092	308	476	240	1243	280	632
293	1075	314	467	280	1145	240	606
282	1028	320	448	101	1140	311	577
320	997	282	427	76	1122	101	526
102	992	102	425	106	1053	307	525
308	912	120	424	311	987	263	514
314	902	291	413	54	986	106	506
51	884	50	404	132	977	76	500

The automated scintillation detection routine detected phase scintillations on L1 and L2C frequencies on all top ten days of 2014 and 2015. Whereas, the amplitude scintillation on L1 and L2C frequencies was not detected on all the top 10 days of 2014 and 2015 ranked on highest amplitude WSN as mentioned in Chapter 3.

The third contribution is categorizing each scintillation from the previous contribution into only phase, only amplitude or both. The process of detecting time intervals common to both the phase and amplitude scintillations detected by the automated scintillation detection is described in Chapter 4, which constitutes the third contribution of this thesis. The algorithm developed to check for common time between the amplitude and phase scintillation on a day did result in a few days in 2014 and 2015 when both the scintillations occurred.

The last contribution of this thesis, which is the main objective of this research, is to identify the ionospheric region irregularity associated with any given scintillation event. The two algorithms based on PFISR and ASC respectively, to identify the ionospheric irregularity is described in detail in Chapter 5. The algorithms are applied to the scintillation events detected and classified by the second and third contributions respectively, and the irregularity region associated with them are identified.

Table 6.2 Summary of a subset of detected scintillations from 2014 and their irregularity region.

Event No	DOY	Year	Frequency	PRN	Start Hour	Start Min	End Hour	End Min	Scintillation Type	Layer
1	282	2014	L1	10	9	1	9	14	only phase	F
2	320	2014	L1	30	9	11	9	25	only phase	E
3	320	2014	L1	32	0	59	1	25	both	F
4	326	2014	L1	14	22	29	22	49	only amplitude	F
5	308	2014	L2	30	9	54	10	9	only phase	F
6	314	2014	L2	17	12	54	13	8	only phase	F
7	320	2014	L2	30	9	12	9	25	only phase	E
8	320	2014	L2	1	1	0	1	15	both	F

6.2 Future Work

6.2.1 Automated scintillation database. In future, all the processes of detecting the scintillation, categorizing its type, and identifying the region of irregularity associated with scintillation will be automated daily. Therefore, a complete scintillation database which records all the scintillation events occurring every day can be generated. The database includes all the information regarding a scintillation event such as day, frequency, scintillating time, scintillating PRN, its category, and the irregularity region associated with that event.

6.2.2 Study of properties of E and F irregularities. From this thesis, only the irregularity region which is causing a scintillation event is identified. With this knowledge the properties of the irregularities present in the E and F regions can be further studied. Previously, SAGA was used to estimate the height and thickness of scattering layer. This can be validated with the PFISR and ASC results as shown here. Future research will examine how the irregularities are varying between the E and F regions, and what the causes for these variations between the two regions are.

BIBLIOGRAPHY

[1] Y.Su, “Kilometer-spaced GNSS array for ionospheric irregularity monitoring,” Ph.D. dissertation, Dept. of Mech. Matl. And Aerospace Eng., Illinois Institute of Technology, Chicago, IL, 2017.

[2] S. Datta-Barua, Y. Su, K. Deshpande, D. Miladinovich, G. S. Bust, Hampton, D., & G. Crowley, “First light from a kilometer-baseline Scintillation Auroral GPS Array,” *Geophysical Research Letters*, vol. 42, no. 10, pp. 3639–3646, 2015, 2015GL063556. [Online]. Available: http://doi.org/10.1002/2015GL063556.

[3] J. Semeter, S. Mrak, M. Hirsch, J. Swoboda, H. Akbari, G. Starr, V. Pankratius, (2017). “GPS signal corruption by the discrete Aurora: Precise measurements from the Mahali experiment.” *Geophysical Research Letters,* vol. 44, pp. 9539–9546. [Online]. Available: https://doi.org/10.1002/2017GL073570.

[4] D. Loucks, S. Palo, M. Pilinski, G. Crowley, I. Azeem, and D. Hampton (2017), “High-latitude GPS phase scintillation from E region electrondensity gradients during the 20–21 December 2015 geomagnetic storm,” *J. Geophys. Res. Space Physics*,122,7473–7490, doi:10.1002/2016JA023839 [Online]. Available: https://doi.org/10.1002/2016JA023839.

[5] Bredk. (2007, May) Layers of the atmosphere. [Online]. Available: https://commons.wikimedia.org/wiki/File:Atmospheric_Layers.svg. [Accessed February, 2018].

[6] D. Anderson and T. Fuller-Rowell. (1999) Various layers of the ionosphere and their predominant ion populations are listed at their respective heights above ground. The density in the ionosphere varies considerably, as shown. [Online]. Available: NOAA: http://www.sel.noaa.gov/info/Iono.pdf

[7] Computational Physics, Inc., The effects of the ionosphere on GPS signals. GPS signal refraction is caused by ionospheric irregularities that produce variations in signal group delay and phase advance. Signal diffraction is caused by ionospheric scattering of signals resulting in radio waves reaching receivers via multiple paths thereby causing fluctuations in signal amplitude and phase. Both refractive and diffractive effects on GPS signals are referred to as scintillation. [Online]. Available: https://www.cpi.com/expertise/projects/past-projects/space-weather/ionospheric scintillation/. [Accessed March, 2017].

[8] SBAS Ionospheric Working Group, “Effect of Ionospheric Scintillations on GNSS – A White Paper,” November 2010. [Online]. Available: http://web.stanford.edu/group/scpnt/gpslab/website_files/sbas-ion_wg/sbas_iono_scintillations_white_paper.pdf. [Accessed April,2018].

[9] S. Datta-Barua, Space Weather Lab at Illinois Institute of Technology. [Online]. Available: http://apollo.tbc.iit.edu/~spaceweather/live/?q=SAGA.

[10] Advanced Modular Incoherent Scatter Radar, October 2007. [Online]. Available: http://isr.sri.com/iono/amisr/news-archives/archives.html.

[11] D. Hampton, University of Alaska at Fairbanks, April 2018. [E-mail].

[12] S. Datta-Barua, Space Weather Lab at Illinois Institute of Technology. [Online]. Available: http://apollo.tbc.iit.edu/~spaceweather/live/uriel_test/eachdate.php?page=2018-3-2

[13] UC Regents. (2006, April) Aurorae are caused by charged particles from inside the magnetosphere and then speed up to very high speeds as they barrel down along magnetic field-lines into the upper atmosphere. As they collide with the gas, they excite the atoms/molecules, which emit light when they relax from the excited state. [Online]. Available: https://www.nasa.gov/mission_pages/themis/auroras/sun_earth_connect.html. [Accessed April, 2018].

[14] University of Alaska at Fairbanks. [Online]. Available: http://ffden-2.phys.uaf.edu/211.fall2000.web.projects/Christina%20Shaw/AuroraColors.html. [Accessed April, 2018].

[15] Madrigal Database at SRI International. [Online]. Available: http://isr.sri.com/madrigal. [Accessed September, 2017].

[16] Geophysical Institute of University of Alaska Fairbanks. [Online]. Available: http://optics.gi.alaska.edu .[Accessed February, 2018].

[17] T.F.Tascione, *Introduction To The Space Environment*. Malabar, FL: Krieger pub., January 1994.

[18] University Corporation for Atmospheric Research - Center for Science Education, “The Ionosphere”. [Online]. Available: https://scied.ucar.edu/ionosphere. [Accessed April 2018].